States of in-situ stress in the Duvernay East Shale Basin and Willesden Green of Alberta, Canada: variable in-situ stress states effect fault stability

Luyi W. Shen[1,2*], Douglas R. Schmitt[1†], Ruijia Wang[4], Tyler E. Hauck[2]

[1]Institute of Geophysical Research, Department of Physics, University of Alberta, Edmonton, Canada

[2]Alberta Geological Survey, Alberta Energy Regulator, Edmonton, Alberta, Canada

[†]Now at Department of Earth, Atmospheric and Planetary Science, Purdue University, West Lafayette, Indiana, U.S.

[4]Department of Earth and Planetary Science, University of New Mexico, Albuquerque, U.S.

[*]Corresponding author: Luyi W. Shen (luyi@ualberta.ca)

Key Points:

- We quantify the in-situ stress in two regions of the Duvernay Formation with active hydraulic fracturing and emerging induced seismicity.
- Elevated fluid pressure likely caused the M_W 3.8 earthquake in the East Shale Basin Duvernay; fault is unstable at natural P_P.
- States of the effective stress control the seismic susceptibility of studied areas.

Abstract

Induced earthquakes in some areas of the Duvernay Formations (i.e., of areas near the city of Red Deer and Fox Creek) due to Hydraulic fracturing (HF) operations nearby and seismic quiescence of the other areas (of a similar level of HF activities) warrants geomechanical investigations. Here, we start by quantitatively constraining the magnitudes and orientations of minimum (S_h), maximum (S_H) horizontal stresses, vertical stress (S_V) utilizing both borehole measurements and earthquake's focal-mechanism (FM) solutions for a study area where a newly emerging swarm of HF induced earthquakes are reported (near the city of Red Deer, Canada). The apparent pore pressures (P_P) are also assessed through several transient well testing results targeting the unconventional reservoirs. This knowledge allows the fault stabilities for the high-profile HF induced Red Deer (M_L 4.2/M_W 3.8) earthquake to be assessed. The N-S (or E-W) aligned fault, revealed by the FM solution, appears to be stable at a hydrostatic fluid pressure but unstable when fluid pressure is increased to the level of ambient unconventional reservoir pore pressures. The slip-tendency of the faults in the region studied is assessed by calculating the required fluid pressures to activate hypothetical faults; we find that the HF-induced clusters geographically overlap with the zones of higher susceptibility. High ambient pore pressure does not correlate with high susceptibility, and large deviatoric stress is needed to cause HF-induced earthquakes.

1 Introduction

Globally, high profile anthropogenically-induced earthquakes (up to M 5 near densely populated areas) in the past decade had brought much attention to the risk and hazards associated with the injection [e.g., hydraulic fracturing, *R Schultz et al.*, 2020, waste disposal, *Hincks et al.*, 2018, geothermal, *Eberhart-Phillips and Oppenheimer*, 1984] and, to a lesser extent, extraction of masses [e.g., *Maury et al.*, 1992; *van Thienen-Visser and Breunese,* 2015; *Wetmiller*, 1986] into/from the subsurface. Extensive efforts had been expended, mainly through the lenses of seismology, with various triggering mechanisms proposed, investigated, and validated. Nevertheless, these reports, primarily statistical in nature, attempt to forensically correlate earthquakes temporally and spatially with industrial activities. There are very few exceptions that are developed on the basis of the deterministic geomechanical observations [e.g., *Deng et al.*, 2016; *McClure and Horne,* 2011; *Shen et al.*, 2019b; *Stork et al.*, 2018]. Despite the elevated societal concerns, only a small fraction of the HF operations results in moderate earthquakes (M > 2). Loosely, these wells associated with this seismicity are classified as being 'seismogenic' [e.g., *Atkinson et al.*, 2016; *R Schultz et al.*, 2018]; the absence of triggered earthquakes in a majority of other HF wells are attributed to the varying geological conditions.

To the date, the cause of such discrepancies is not yet well understood, but this is not surprising as statistical correlation requires the input of past earthquake records that would be absent for aseismic areas. Techniques similar to the Probabilistic Seismic Hazard Analysis (PSHA), which relies on establishing statistical or empirical patterns of reported earthquake events [*Castaños and Lomnitz*, 2002], are adopted to perform susceptibility analysis for large landmasses. Nevertheless, PSHA had demonstrated deficiencies with striking examples of Tohoku earthquake (M 9.1, 2011), Wenchuan earthquake (M 7.9, 2008), Haiti earthquake (M 7.0, 2010) that happened in areas mapped, often owing to their relative prior seismic quiescence, as lower risk [*Stein et al.*, 2012]; these events generated heated debate [e.g., *Frankel*, 2013].

An alternative and more deterministic alternative approach to assessing seismic risk, particularly in areas that historically have been aseismic, is to evaluate the stability of candidate faults using knowledge of the state of stress and fluid pressures. Such studies are currently needed for both the purpose of understanding the risk of induced earthquakes and comparing them with statistical susceptibility maps to test the objectivity [*Stein et al.*, 2011]. The growth of deep waste fluid disposal and large-scale hydraulic fracturing for both geothermal and hydrocarbon resources motivates further development of more direct assessments, particularly in areas that are historically aseismic.

Under the framework of the Mohr-Coulomb friction law, a fault slips along a plane once the shear traction resolved onto the failure plane exceeds the frictional resistance – resolving this requires complete knowledge of the in-situ stress tensor, the pore fluid pressures, and the coefficient of friction. Although the principle is relatively straightforward, conducting such an analysis in practice can be problematic as the state of stress is often poorly constrained. To obtain representative stress values, nearly all of the studies that attempt to quantitatively assess the stability on faults are forced to make numerous assumptions; these often include the use of estimates of stress and pore pressure gradients, reliance on frictional constraints along hypothetical optimally oriented, critically-stressed, faults, or application of the lateral constraint concept. The values provided by such methods may deviate significantly from those actually exist within the Earth's interior; particularly, the use of the lateral constraint assumption may mislead [e.g., *Ong et al.*, 2016]. More accurate stress field information can only be reliably obtained from deep boreholes. Consequently, the state of stress is best constrained by different but complementary measurements, and the economic costs associated with obtaining this information can be prohibitive. If stress field data are, however, available, it should be used as one component of a risk assessment in areas with low or nonexistent historical seismicity.

Until recently, this situation existed in the Western Canada Sedimentary Basin (WCSB), but since 2010, a number of induced earthquakes have been linked to multistage hydraulic fracturing for hydrocarbons primarily within the high-organic bearing Devonian marine sedimentary formations. While only less than 2 percent of these wells are reportedly seismogenic (even less if vertical HF wells are to be included [*Atkinson et al.*, 2016]), a series of $2.5 < M_L < 4.7$ earthquakes occurred within a small area near the town of Fox Creek, Alberta including some felt by the local residents. These events have been extensively studied (see review in *R Schultz et al.* [2017]) - spatially and temporally linked to the HF operations of individual wells in the hydrocarbon-rich Duvernay Formation. Mitigation efforts included implementing a traffic light protocol [*AER*, 2015] that was enforced once events of $M_L > 4$ occurred [*Shipman et al.*, 2018]. These induced earthquakes also motivated an extensive analysis of borehole-logging and pressure-testing data [*Shen et al.*, 2018; 2019a], leading to the construction of a quantitative model for the stress tensor over the Fox Creek area that was then applied in understanding the conditions for stability/instability along the rupture planes for 11 of the largest induced events [*Shen et al.*, 2019b].

Since 2012 an area to the south of the Fox Creek events and with comparable geological structure (see **Figure 1a**) also experienced high levels of the HF activities into the target Duvernay Formation [*BMO*, 2019]. However, the areas near the city of Red Deer appeared to be seismically quiescent and was consequently mapped by *Pawley et al.* [2018] as low risk in comparison with the Fox Creek area to the north; this difference in seismic activities initially motived, for the purposes of comparison, development of the quantitative stress model described here. This quiescence ended, however, with two events felt by the local residents in March 2018 and March 2019. The M_L 4.2/M_W *3.8* earthquake (Mar 4, 2019) near the city of Red Deer triggered a new traffic light protocol [*AER*, 2019], followed by the shut-in of the suspected seismogenic wells. Earthquakes with smaller magnitudes (< 2.5) are also reported in the nearby

Willesden Green (WG) area of the Duvernay play in the West Shale Basin (WSB). More recently, intensive studies of existing seismic data revealed additional small clusters, some of which are likely natural but many associated with HF operations since 2014 [*R Schultz and Wang*, 2020]. In contrast, HF wells in portions of the East Shale Basin (ESB, i.e., Ghost Pine Embayment and most of the WG) remain non-seismogenic up to the date of this writing.

Here, to better understand the seismicity and seismic quiescence in this zone, we construct a quantitative model for the state of 3D-stress and formation pore-fluid-pressure for the Duvernay Formation. Our approach follows strategies developed earlier for the Fox Creek area [*Shen et al.*, 2019a; *Shen et al.*, 2019b]. We first review the current knowledge of geological structure, levels of seismicity, and the state of stress in this area of Alberta. We briefly overview the methodologies used in developing the stress model, focusing more heavily on those employed in constraining the magnitude of the greatest horizontal compression S_H. This final model is then applied in understanding, first, the factors affecting the stability of the 2019 events and, second, in the mapping the susceptibility for seismicity over the area. The paper concludes with thoughts regarding the mechanisms triggering induced seismicity in this area.

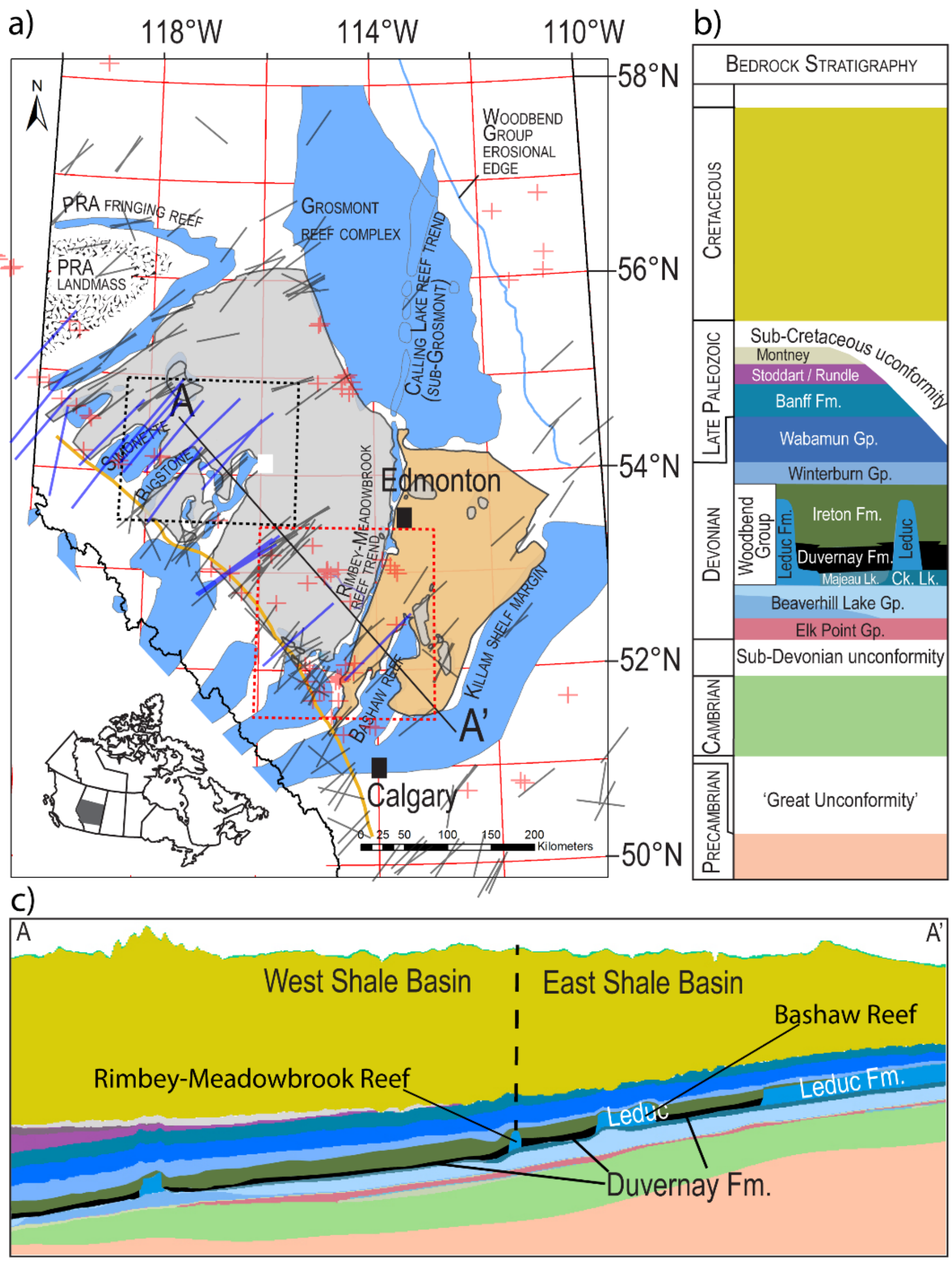

Figure 1. **a)** Overview of the study area in Alberta, Canada with previously reported stress directions from World Stress Map [WSM, gray dashes, *Heidbach et al.*, 2016], *Shen et al.*, [2018, blue lines] and locations (red crosses) of reported S_h measurements from *Haug and Bell* [2016]. The grey and light orange zones represent the spatial extent of the Duvernay Formation

in the West Shale Basin (WSB) and East Shale Basin (ESB), respectively, that are separated by the Rimbey-Meadowbrook reef trend. The black box represents the aerial extent of the inset map **Figure 3**. The black dashed boxes represent the study area in [*Shen et al.*, 2018], and the southern red dashed box is the current study area. The yellow line denotes and Cordilleran Deformation Front (CDF). **b)** Bedrock stratigraphy of western central Alberta with elements from the cross-section shown in **c)** for the line A-A' in a). Vertical depth in c) is exaggerated by 50 times.

2 Background

The ~200 km × 200 km study area (**Figure 2**) includes the city of Red Deer that is a few tens of kilometers to the east of a moderate HF induced earthquake (M_W 3.8/M_L 4.2, [*R Schultz and Wang*, 2020]) referred to hereafter as the *Event A* (**Table 1**). HF activities occur within the Duvernay Formation that is bisected by the Rimbey-Meadowbrook Reef Trend (**Figure 1, 2a**) into areas referred to as the WSB in gray and ESB in tan [*Preston et al.*, 2016]; the portions of the WSB and ESB are, respectively, within the Edson-Willesden Green (WG) and the Innisfail Regulatory Assessment Areas [*Preston et al.*, 2016]. The Bashaw Reef complex extends NE into the ESB, separating the Westerdale and Ghost Pine Embayments. The depth of the Duvernay Formation increases significantly from NE to SW (**Figure 2b**) due to its steep dip and increasing surface topography westward (**Figure 2b**). The Cordilleran Deformation Front is another important structural element (**Figure 2a**) that separates highly deformed lithologies in the SW from those more gently dipping to the NE.

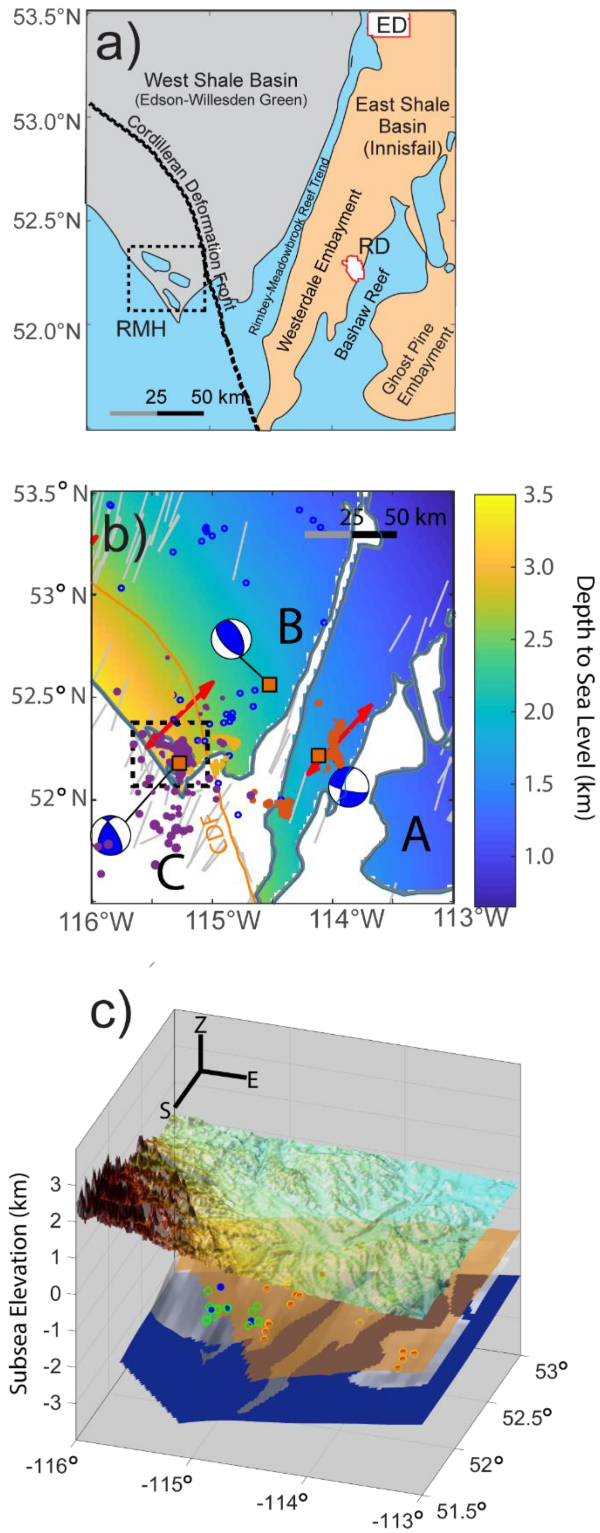

Figure 2. a) Map of major geographic features associated with the Duvernay Formation, including the WSB (including the Edson-Willesden Green Assessment Area) and the ESB

(including the Innisfail Assessment Area). The eastern edge of the Cordilleran Deformation Front (CDF) is indicated by the heavy dashed line. The box RMH contains the Rocky Mountain House Seismic Zone. The cities of Red Deer and Edmonton are shown in white denoted RD and ED, respectively. **b)** Detail map of epicenters within the study area, the background color indicates depths from sea level to the tops of the Duvernay Formation. Outlined brown squares: three major earthquakes designated A, B, and C with FM resolved (**Table 1**); brown dots: induced events in East Shale Basin (ESB), orange dots: events in Williston Green district of West Shale Basin, purple dots: events in Rocky Mountain House Seismic Zone (RMHSZ, delineated by the dashed box) west of the Cordilleran Deformation Front. Blue open circles represent the earlier S_h measurements from *Haug and Bell* [2016] compilation. Grey lines denote the reported stress orientations from the WSB; red arrows for the newly acquired image log for this study and one from *Shen et al.*, [2018]. The orange line is the CDF. Red polygons mark the cities of Edmonton and Red Deer and the town of Rocky Mountain House (RMH). **c)** 3D view of the study area, comprising in stratigraphically descending order, the surface topography, sub-Cretaceous unconformity (brown), the top of the Duvernay Formation, and the Precambrian basement. Red dots with yellow outlines represent the locations of S_h and P_p measurements within the Duvernay Formation reported in [*Shen et al.*, 2018] and this study. Blue dots and open green circles represent previously reported S_h and P_P in the shallower/younger Cretaceous-aged strata from *Haug and Bell* [2016] and *McLellan* [1989].

2.1 Geological framework

The broad sedimentary stratigraphy (**Figure 1b**) is underlain by Paleoproterozoic metamorphic and igneous rocks and is comprised of: 1) a thick succession of Paleozoic to lower Mesozoic carbonates, shales, and evaporites deposited predominantly during tectonic quiescence, and 2) an upper succession of Mesozoic basin-filling siliciclastics that formed in response to orogenesis along the western margin of North America. Orogenesis initiated in the Late Jurassic (163 Ma) and continued through to the Eocene (52.1 Ma), punctuated by periods of tectonic quiescence [*Pană and van der Pluijm*, 2015]. Significant unconformities separate the sedimentary successions from the underlying crystalline rocks and within the sedimentary succession between phases 1 and 2. Here, we provide a brief overview of the local structure with a focus on those elements that possibly relate to faults in the study area.

Precambrian basement rocks in the WCSB comprise a number of Archean- to Paleoproterozoic-aged tectonic provinces [*Ross and Eaton*, 1999; *Ross et al.*, 1991] (**Figure 3a**). The Archean portion of the basement represents the oldest and most stable part of the cratonic rocks that make up the core of North America. Younger rocks were welded to the Archean crust in the Paleoproterozoic during accretionary and collisional processes [*Hoffman*, 1988]. The Precambrian tectonic domains within the study area were delineated through potential field maps and U-Pb geochronology from basement samples taken from drill-cores [*Burwash et al.*, 1994; *Ross and Eaton*, 1999; *Ross et al.*, 1991]. A prominent feature in potential field data is the NE-trending Snowbird Tectonic Zone, which bisects the basement in the northwestern part of the study area (**Figure 3**). Another prominent basement feature can be seen on LITHOPROBE 2D seismic profiles that cut through the NE section of the study area, where they show a strong subhorizontal reflector interpreted as an abrupt change in metamorphic facies [*Bouzidi et al.*, 2002] or as regional sills at about 15 to 20 km depth. A series of reflectors with an apparent westward dip of about 45° are readily in the uppermost metamorphic crust. Interestingly, an abrupt 10 km change in the topography of the Mohorovičić discontinuity has also been interpreted [*Bouzidi et al.*, 2002] that hints at tectonic motions in the distant past.

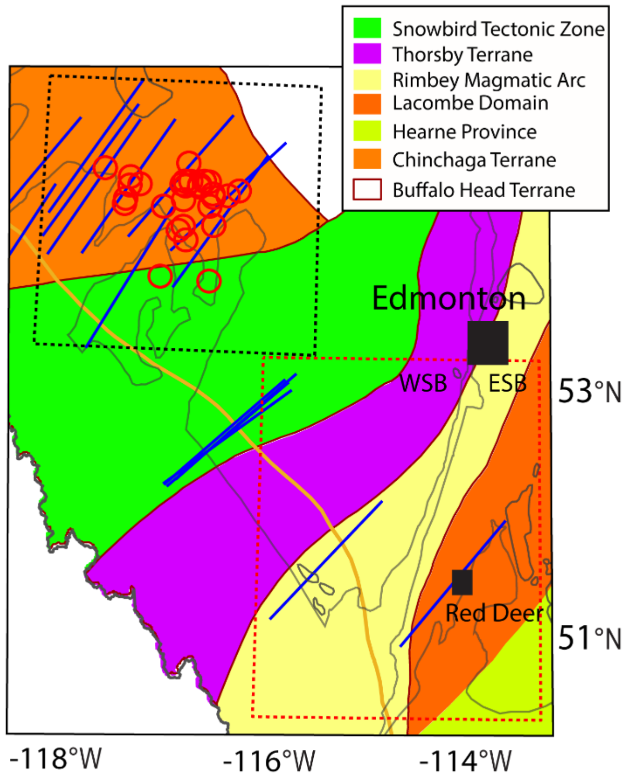

Figure 3. Geological features of our study are with a) map of the tectonic provinces mapped by *Ross et al.* [1991] with the lines reproduced in *Gu and Shen* [2015] and stress measurements reported in *Shen et al.* [2018]. Blue lines show the directions of S_H from both this study and *Shen et al.*, [2018]. Red circles denote the locations of S_h measurements in *Shen et al.*, [2019a]. The yellow line denotes the Cordilleran Deformation Front.

Despite the clear features revealed in the crustal-scale seismic-reflection profiles, there is little clear evidence for any large-scale tectonic reactivation within the Precambrian basement. Nevertheless, numerous studies (see recent review in *Corlett et al.* [2018]) have used various lines of evidence suggesting that the modest fault displacements of the basement may have influenced the deposition of the Paleozoic sediments. If fault-related displacements of the basement exist in the study area, they remain below the limit of seismic resolution [*Ross and Eaton*, 1999]. For example, *Edwards and Brown* [1999] attempted to relate the 540 km long, suspiciously linear Rimbey-Meadowbrook Leduc Reef trend (see Fig. 1 and 3b) that runs through the study area to possible basement structure, but no relationship was observed. The debate of possible Precambrian basement fault control on the overlying Phanerozoic sediments, however, is longstanding (see *Moore* [1988]).

The top of the Precambrian basement in the study area marks a global event in the form of a nonconformity, known as the 'great unconformity' [*Peters and Gaines*, 2012]. In the study area, the basement is overlain by Middle Cambrian rocks, which are, in turn, overlain by Devonian strata, separated by the sub-Devonian unconformity (**Figure 1a**). Within this assemblage, the Devonian succession comprises a middle Devonian package, of mostly siliciclastics and evaporites, and an Upper Devonian succession of mostly carbonate reefs and intervening basin-filling siliciclastic (**Figure 1d**). The Upper Devonian Duvernay Formation consists mainly of bioturbated siliceous, calcareous, and argillaceous mudstones; it is the main target for HF because of its attractive organic content [*Rokosh et al.*, 2009] and mechanical stiffness. Presently, the Duvernay Formation still retains significant gas and condensate hydrocarbons that motivate exploitation with horizontal drilling and associated hydraulic fracturing.

The Devonian succession is overlain by late Paleozoic strata, the top of which is the sub-Cretaceous unconformity (**Figure 1b** and **2b**). Early Cretaceous siliciclastic sediments overlie the Paleozoic succession in the study area, which were deposited in a foreland basin setting [*Beaumont*, 1981]. The foreland basin was created during flexure of the lithosphere induced from crustal loading initiated by convergent tectonics, commencing possibly as early as the late Jurassic, although the timing is debated [*Chen et al.*, 2019; *Pană and van der Pluijm*, 2015]. The flexure of the Precambrian basement surface and the Paleozoic strata is particularly apparent as an increasing structural dip toward the orogen in the west (**Figure 1d** and **2b**). The easternmost edge of the deformation front falls within the SW corner of the study area.

To the best of our knowledge, there are no currently available reports of pre-existing faults to the east of the Cordilleran Deformation Front within the study area - in stark contrast to the well-known sequence of major thrust faults and complex structures exposed in the fold and thrust belt [e.g., *Price*, 2001] to the south-west of this boundary. Within the subsurface, evidence from seismic-reflection profiles suggest faulting effecting successions from the Paleozoic to Mesozoic: both to the north associated with the Peace River Arch [e.g., *Weides et al.*, 2014] (Fig. 1a) and to the south [e.g., *Galloway et al.*, 2018; *Lemieux*, 1999]. Additionally, to the north near Fox Creek, the existence of faults has been inferred from various interpretations of seismic reflection data and its attributes [e.g., *Chopra et al.*, 2017; *Corlett et al.*, 2018; *Eaton et al.*, 2018; *Ekpo et al.*, 2017; *Weir et al.*, 2018]. Sedimentation patterns and accommodation trends within the basin could also be indicative of differential vertical displacements. For example, to the north of our study area, syndepositional motion along faults related to the Snowbird Tectonic Zone may have resulted in anomalous localized thickening of the Albian Viking Formation [*S Schultz et al.*, 2019].

2.2 Regional seismicity: natural and induced

Prior to 2014, the study area has experienced low levels of seismicity, with only 35 cataloged events above M_W 2.5 since 1960 [*USGS*, 2020]. Many of these are associated with a cluster occurring in the SW part of the study area (**Figure 2a**) possibly related to natural gas production during the 1980s, in a region that was consequently referred to as the Rocky Mountain House Seismic Zone (RMHSZ) [*Rebollar et al.*, 1982; *Wetmiller*, 1986]. Slightly to the west of our study area (~W116.20º, N52.75º), wastewater-injection-induced earthquakes have been reported at the Cordel Field [*R Schultz et al.*, 2014] with M_L < 4 in the early 2000s. It should be noted, however, that the RMHSZ and Cordel Field events are all located to the SW of the Cordilleran Deformation Front in a highly faulted and fractured rock masses thrust upwards during the orogeny that produced during the formation of the Rocky Mountains.

The less deformed area to the NE of the Cordilleran Deformation Front was considered seismically quiescent until the 3.8 M_W (M_L 4.2 Event A) and 3.1 M_L events occurred in the ESB on Mar 4, 2019 and Mar 9, 2018 respectively. The source parameters of the M_L 3.1 (Mar 9, 2018) earthquake were poorly constrained – owing to the sparse seismometers network near the epicenter at the time. However, the larger *Event A* and later deployed dense seismometer array, deployed after the M 3.1 event [*R Schultz and Wang*, 2020], allowed for accurate FM determination; subsequently, an intensified search in the area detected > 1200 additional earthquakes in the Westerdale Embayment from 2014 to 2019 with magnitudes of M_L -0.7 – 4.3 [*R Schultz and Wang*, 2020]. Temporal and spatial associations are highly correlated with HF activities in the ESB that commenced in 2012 [*BMO*, 2019]. Meanwhile, the other well-developed HF sites (i.e., north of the city of Red Deer, the Ghost Pine Embayment, and most of the WG) have remained quiescent (see **Figure 2a**).

It is also important to note the occurrence of an M_W 3.9 (M_L 4.3) earthquake (*Event B*) at a depth of 15 km in the NW corner of the study area on Mar 10, 2019 (**Figure 2a**). This event's mid-crustal depth, its reverse fault FM, and its distances to any HF activity diagnosed it as a natural event [*R Schultz and Wang*, 2020].

Table 1. Significant Seismic Events in the Area and Relation to Stress Field

			Conjugate Plane Orientations					Andersonian Stress				
									Principal Components (MPa)			
Event	Date M_W	Epicenter Depth	Plane	Strike	Dip	Rake	Azimuth ϕ	S_h	S_V	S_H *(Borehole Failure)*	S_H *(FM inversion)*	P_P
A	03/04/ 2019 M_W 3.8	N52.20° W114.11° 2.5 km	1	101°	72°	-30°	N47°E	46	61	75 – 116	65 -106 (median: 84)	40
			2	201°	62°	- 160°						
B	03/10/ 2019 M_W 3.9	N52.57° W115.26° 15 km	1	138°	49°	77°	N52°E	-	-	-	-	-
			2	338°	42°	105°						
C	10/19/ 1996 M_W 3.4	N52.21° W115.25° 5.2 km	1	205° *156°†*	44° *44°†*	136°	N50°E	110	132	132 - 155	-	-
			2	329° *302°†*	61° *51°†*	55°						

†. Alternative FM analysis attributed to R. Horner as provided in Baranova et al, 1998.

2.3 Regional state of stress

We assume an Andersonian [*Anderson*, 1951] state of stress, where it is generally accepted that at a sufficient depth the vertical compression S_V is the principal stress; and by default, the other two principal stresses are the maximum S_H and minimum S_h horizontal compressions. The azimuth direction ϕ of S_H then provides enough information to complete the total stress tensor [e.g., *Schmitt et al.*, 2012]. When necessary to depart from the Andersonian assumption, the three principal compressions are denoted $\sigma_1 > \sigma_2 > \sigma_3$. Further determination of the formation rock's pore fluid pressure P_P is necessary for calculating effective stresses and understanding potential rock failure. In this writing, fluid pressures and compressive stresses are assigned with positive signs following standard conventions in the geosciences.

While here we are interested in the absolute magnitudes of the principal stresses, one complication is that, in engineering practice, 'stress gradients' are usually reported. These are the secant gradient that is simply calculated as the ratio of a single measurement of stress magnitude S or pressure P to the depth z at which the measurement is made. The most common of these is the 'fracture gradient' S_h/z that allows drilling engineers to make rapid calculations of stress conditions – but, later finding the actual S_h magnitude at a given location then requires one to know the depth. Following *Shen et al.* [2019a], a tangent gradient is the slope of a linear fit to the measurements of the given parameter (e.g., S_h and P_p) as a function of depth within the same geological formation (e.g., Duvernay). Within the Duvernay Formation, this tangent gradient differs significantly from the secant gradient. Obtaining a tangent gradient, however, requires the luxury of having numerous measurements in a given area.

Earlier studies on the states of in-situ stress for the Alberta Basin started with the identification of borehole elongation measured with caliper logs [*Bell and Gough*, 1979] with a more recent review by *Reiter et al.* [2014]; these data are incorporated in the latest version of the Word Stress Map [WSM, *Heidbach et al.*, 2016] and included in the *Haug and Bell* [2016] compilation. In addition to the latest compilation of the WSM, 20 borehole images with identified borehole breakouts (BO) and drilling-induced tensile fractures (DITF) were recorded in a published dataset [*Shen et al.*, 2018]. These studies all broadly show a relatively uniform

NE-SW compression across the Alberta Basin; as such ϕ is expected to be ~45° in our study area.

It is usually assumed that S_h magnitudes can be measured directly in certain transient pressure tests by finding the borehole pressure P_{fc} at which a small induced hydraulic fracture closes. These tests are variously called extended leak-off tests, micro-fracture tests, mini-fractures tests, and diagnostic fracture injection test (DFIT), with this latter term currently usually used for all such tests (see discussion of the methods in *Shen et al.* [2018]). *Bell and Caillet* [1994] compiled 106 S_h measurements (39 within this study area, see **Figure 2b**) from tests in the Mesozoic hydrocarbon reservoirs. *Haug and Bell* [2016] have updated these data by incorporating results from later studies [*Bell and Bachu*, 2003; *Bell and Grasby*, 2012; *McLellan*, 1989; *Woodland and Bell*, 1989]. Their results are reported as average secant S_h gradient of ~19 kPa/m. *McLellan* [1989] also reported 16 formation pore pressure P_P measurements and 4 S_h measurements, which had not been included in other published stress-data compilations. More recently, *Shen et al.* [2018] reported 38 S_h measurements from recently conducted tests in the Duvernay Formation, including 12 measurements in our study region that provided an average secant gradient of ≈ 21 kPa/m, but if analyzed together as a set plotted with depth, indicated a tangent gradient $\Delta S_h(z)/\Delta z \approx 32$ kPa/m.

No reliable method to directly measure the S_H magnitudes from deep boreholes yet exists; it can only be constrained. *Shen et al.* [2019a] attempted to overcome this limitation in the Fox Creek area by combining the measured values of S_h and S_V with the 'shape factor' [*Bott*, 1959] derived by inverting the local FM to provide constrained S_H distribution; efforts had also been expended with borehole failures identified by examining the image logs [*Shen et al.*, 2018]. These inversions, too, show σ_2 is close to vertical in agreement with the Andersonian assumptions and indicating a strike-slip faulting environment at least within the Duvernay Formation.

2.4 Estimating Fault Stability

The initiation of rupture along a plane of weakness is presumed to be governed by the Mohr-Coulomb frictional criterion that may be used to assess the stability or slip-tendency of an arbitrarily oriented plane of weakness [e.g., *Morris et al.*, 1996]. This is accomplished by resolving the stress tensor into its effective component tractions normal ($\sigma - P_f$) and tangential (τ) to the plane of interest (see *Schmitt* [2014] for a review). The criterion is expressed, following the *Morris et al.* [1996], with a shear-to-normal ratio (*SNR*)- slip is expected once the friction on the surface is overcome

$$\mu < \frac{\tau - C}{\sigma - P_f} \equiv SNR \tag{1}$$

In Eqn. 1 we retain the cohesion *C*, which most authors dispense with, but as shown in *Shen et al.* [2019b], does noticeably influence the slip-tendency of the plane of weakness. Also, in this simplified form, a static frictional coefficient μ controls the ratio between shear friction and normal traction acting on the surface. P_f should be considered as the fluid pressure active at the plane of weakness where slip occurs; it is sometimes omitted in many studies. For reasons discussed later, it is important to distinguish it from the ambient pore pressure P_P measured from boreholes within the Duvernay Formation (see *Shen et al.* [2019b]).

Despite the simplicity of Eqn. 1, direct quantitative analysis of the slip-tendency of faults remains rare, largely owing to the difficulties in obtaining reliable quantitative stress magnitudes and fluid pressures [e.g., *Schwab et al.*, 2017]. In areas where borehole access is not available, researchers often invert the geometries of the FM [*Michael*, 1984; *Vavryčuk*, 2014] to constrain regional average stress orientation, where the principal stress magnitudes are described relatively by the shape factor ratio *R*:

$$R = \frac{\sigma_1 - \sigma_2}{\sigma_1 - \sigma_3} \tag{2}$$

The *R* determined in inversions gives only the relative deviatoric components of the stress tensor, but in a strike-slip faulting environment, it does allow S_H to be calculated if S_V and S_h are independently found [e.g., *Hardebeck and Hauksson*, 2001; *Shen et al.*, 2019a]. This will be applied here also to constraint S_H from one of the well-known FM observed.

3 Data and Quantitative 3D Stress Model

In this study, we develop a model that quantitatively predicts the states of stress for a crustal volume that encompasses the Duvernay Formation within the study area (**Figure 2**). Stress orientation ϕ and Andersonian principal stress magnitudes: S_h, S_V, and S_H, are constrained by incorporating various well-logging data and transient well-testing results.

Details of the analysis, much of which employs methods similar to that used in the earlier study of the Fox Creek area [*Shen et al.*, 2018; 2019a], is supplied in the electronic supplement (see Text S1, S2, and S3). To summarize, however:

i. Stress orientations ϕ are obtained from an analysis of breakout and drilling induced tensile fractures observed in one newly analyzed image log (Lat: 52.281062, Lon: -113.962146) near the city of Red Deer combined with earlier compilations [*Reiter et al.*, 2014; *Shen et al.*, 2019a]. Our confidence in the areas within the extent of the Duvernay Formation is generally high with stress orientations to the northeast (average ϕ ~ 48°), which agrees with previous studies at much larger scales [*Reiter et al.*, 2014]. Comparatively, the stress orientation to the north in the Fox Creek area of *Shen et al.* [2019a] shows a similar NE stress orientation averaging 45°. The measured values are interpolated over the study area according to inverse distance weighting to produce a ϕ map (**Figure 4a**) with its associated confidence (**Figure 4b**, see Text S1 for details).

ii. S_V magnitudes are calculated by integration with the depth of the density logs while corrected using the Green's function method of *Liu and Zoback* [1992] to account for variations in the surface topography (see Text S2 for details). The map of the interpolated S_V magnitudes at the top of the Duvernay Formation is shown in **Figure 4c** and the corresponding uncertainties in **Figure 4d**.

S_h magnitudes are determined from the analysis of transient pressure records that includes 8 new analyses and 12 from *Shen et al.* [2018]; and formation pore fluid pressures P_P are determined with 22 records from *Shen et al.* [2018] and 20 newly collected ones. The maps and associated uncertainties, including the zone in which high confidence is placed in the values, are shown in **Figure 4e-h** (see Text S3 for details).

Further, all of the available local S_h and P_P from measurements in the Mesozoic [*Haug and Bell*, 2016; *McLellan*, 1989] and more recent Duvernay [*Shen et al.*, 2018; 2019a] compilations are plotted versus depth (**Figure 5**). Linear regression of S_h vs. z (see **Figure 5a**) gives

$$S_h(z) = 22.2 \pm 5.6 \frac{kPa}{m} z - 12.8 \pm 3.4\, MPa \tag{3}$$

while a similar analysis for P_P vs z (see **Figure 5b**) yields:

$$P_P(z) = 24.8 \pm 3.6 \frac{kPa}{m} z - 6.8 \pm 6.8\, MPa \tag{4}$$

iii. As noted, the determination of S_H is challenging; more efforts are necessary to describe its constraint using first, values obtained from the observed borehole breakout dimensions (see details in section 3.1), and second, from inversion of the M_W 3.8's FM solution (Event A, see details in section 3.2).

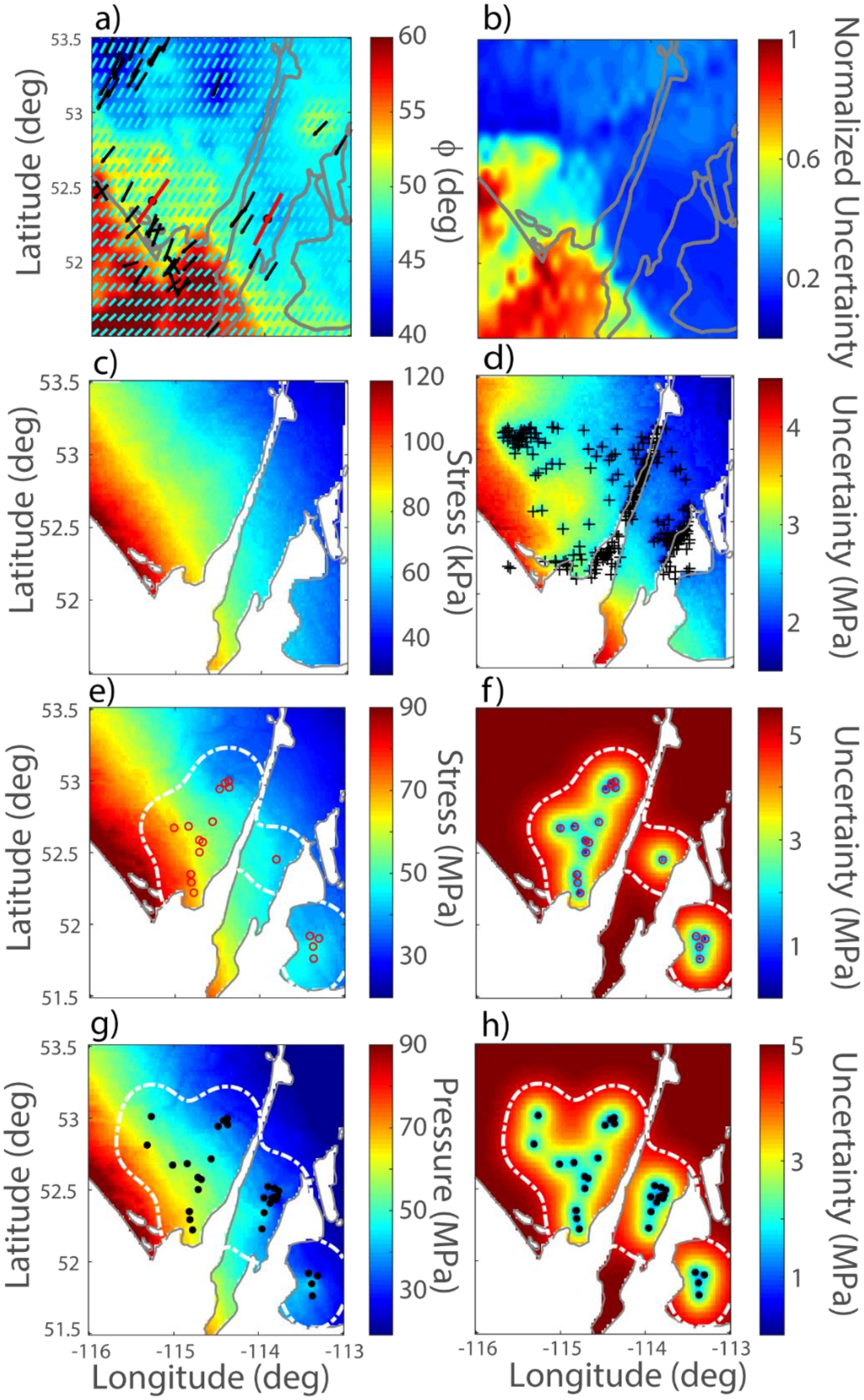

Figure 4. Spatial maps for the states of stress in the center of the Duvernay Formation of our study area. **a)** the orientation of S_H and **b)** normalized uncertainty (from 0 - 1) (see *Shen et al.* [2019a] and supplementary material for details); black dashes represent the measurements reported in WSM; red lines represent the measurements from *Shen et al.*, [2018] and this study. Gray lines enclose the areal extent of the Duvernay Formation engulfed by the Leduc reefs. **c)** the magnitudes of S_V and **d)** uncertainty; black crosses show the location of wells where segments of density logs are retrieved for a 3D density model. **e)** magnitudes of S_h and **f)** the uncertainties with the red circles show the locations of measurement points. **g)** and **h)** shows the P_P and their uncertainties measured at the locations denoted by black dots. White contours in e) to h) show the enclosed areas with uncertainties of less than 5 MPa for S_h and 4.5 MPa for P_P.

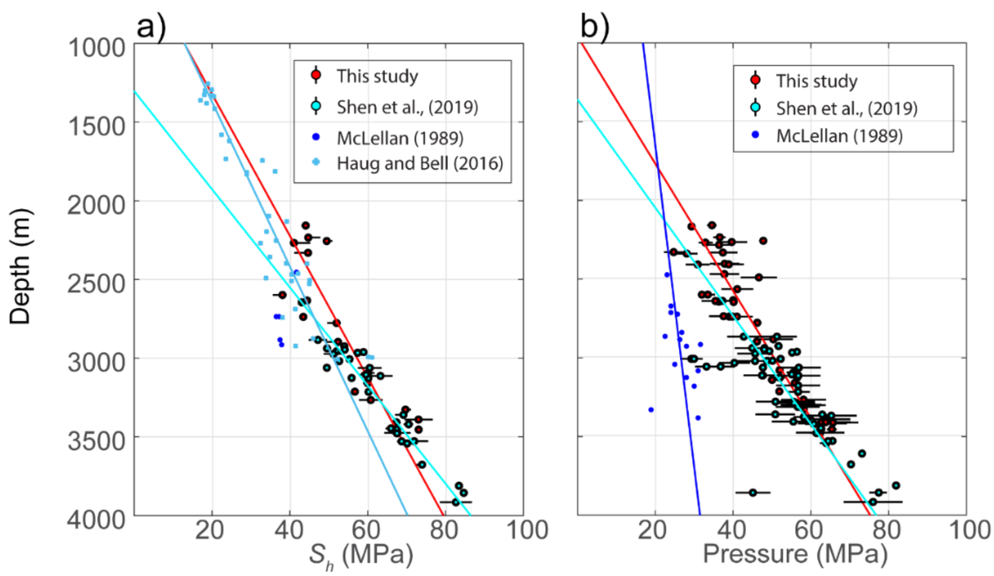

Figure 5. Reported measurements (with their respective uncertainties) and linear regression results for **a)** S_h and **b)** P_P from different sources; see text for details. Locations of the measurement boreholes are shown in **Figure 2** and **Figure 4**.

3.1 Breakout constraints on S_H

The first constraint of S_H relies on the assumption that a borehole breakout is confined to those zones near the borehole, where the state of concentrated stress makes the material unstable to shear rupture. Consequently, the edge of the breakout delimits the zones of stability and instability from one another; the total angular width of the breakout β can provide a constraint on the stress magnitudes. If a simple Mohr-Coulomb failure criterion (Eqn. 1) is employed, S_H may be expressed as [*Valley and Evans*, 2019]

$$S_H = \frac{C_o + \frac{2P_W}{1-sin\psi} - \frac{2P_P sin\psi}{1-sin\psi} - S_h(1-2\cos\beta)}{1+2\cos\beta} \quad (4)$$

where $\psi = \tan^{-1}(\mu)$ is the internal friction angle, C_0 is the unconfined compressive strength, and P_w is the wellbore fluid (mud) pressure. If $P_P = P_w$, this collapses to a form that excludes ψ

$$S_H = \frac{C_o + 2P_P - S_h(1-2\cos\beta)}{1+2\cos\beta} \quad (5)$$

that then, to account for the excess fluid pressure when P_P is different from P_W, matches the values given in as the widely used form

$$S_H = \frac{C_o + 2P_P + \Delta P - S_h(1-2\cos\beta)}{1+2\cos\beta} \quad (6)$$

that $\Delta P = P_w - P_P$ [*Barton et al.*, 1988]; this equation only applies when P_w is close to P_P.

Determination of the exact β value from the image logs collected in this study is also hampered by the lack of access to the raw logs and poor image-scan resolution. Thus, we assigned considerable uncertainty (10 degrees) to the measured BO widths. For smaller or blurry BOs, which the widths are difficult to determine and thus not reported, a range of 0 – 45° is assumed. Further, we also tested a wide range of the rock's compressive strength unconfined compressional strength from 60 to 160 MPa that represent broadly the range reported from a limited number of axial loading tests [*Ong et al.*, 2015]. Owing to the sparsity of the measurement points and large uncertainties, instead of constructing a map, we focused on providing a vertical profile of S_H as a function of depth (z).

Given the relatively high uncertainties associated with this method, we utilized a Monte Carlo (n = 5000) style analysis using randomly selected input parameters for Eqn. 6 and their corresponding uncertainties of: 1. S_h and P_P with predicted by Eqn. 3 and 4; 2. P_W obtained from wells' drilling reports (see supplementary data for details) and 3. ranges of C and β discussed in the paragraph above. A uniform distribution is assumed within the ranges of uncertainties. The median, 25th, and 75th percentiles of the cumulative density function of the calculated S_H distribution are shown in **Figure 6**. Despite the uncertainties, this analysis does give ranges of S_H that are consistent with a strike-slip faulting environment.

Eqn. 6 gives an estimate S_H assuming the P_w is reasonably close to P_P [*Barton et al.*, 1988]. In practice, the validity of this assumption is challenged by a number of factors - most revolve around the pressure difference between the P_P and P_w. Here, we analyzed the borehole images that had also provided constraints on the stress orientation. Due to the limited available data, we also included two more sets of borehole images from locations slight to the west of our study area. Three of the image logs analyzed in this study report the segments of borehole BOs that are observed in the formations from the Cretaceous Glauconite to Cardium Formations (red, purple and green stripes in Fig. 6), with reported P_P of ~24.6 MPa at 2.6 km (expected P_w = ~30 MPa) to ~28.6 MPa at 3.9 km (expected P_w = ~47 MPa) [*McLellan*, 1989]. From the segments of BOs within the Woodbend Group, including the Duvernay Formation (blue stripes in Fig. 7), we observed P_P overpressure of 38.2 MPa (2.5 km deep, expected P_W ~= 30 MPa). It is also important to acknowledge the caveats that the reported P_P from *McLellan* [1989] may not be representative of the virgin state of the reservoir as those measurements were made after extended periods of production. We also do not have knowledge of the P_P in the Ireton Formation shales overlying the Duvernay Formation (**Figure 1d**) because it has not been of economic interest and there are no appropriate measurements within it.

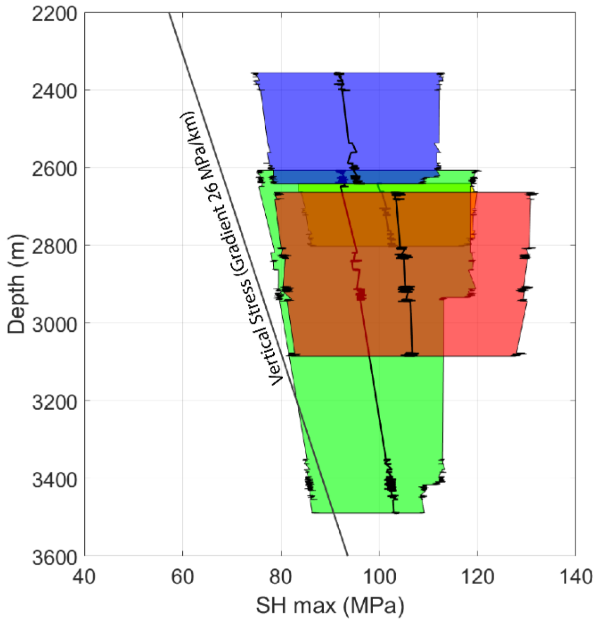

Figure 6. Estimated maximum stress S_H from borehole breakouts. The width of the polygons mark the 25th to 75th percentile of the cumulative probability density functions for S_H, computed using Monte-Carlo methods, and the black lines stand for median values of S_H. Each color of the circles and polygons stand for different boreholes (see text for details).

Despite all the caveats mentioned earlier, we calculated S_H using the same approach for the other three wellbores (see **Figure 6**) for comparison with the results of stress inversion discussed below. It is worth noting that the S_H values obtained from the depth of the Devonian Woodbend Group in the east part of our study area are shallower than those from the younger Cretaceous formations (e.g., Viking, Cardium, Glauconite) in the west because of the westward dipping trends owing to the elevated topography and isostasy within the foreland basin (see

Figure 1d and **Figure 2c**). Regardless, the constraints obtained through both borehole stability analysis reports that S_H can be described roughly as a function of depth:

$$0.0143\,z + 40 \leq S_H(z) \leq 0.0143\,z + 80 \tag{7}$$

for z (depth) ranges between 2200 and 3200 m; the unit of stress is MPa; for 3200m < z < 3600m, owing to the constraint that $S_H > S_V$, we have:

$$S_V(z) < S_H(z) \leq 0.0143\,z + 80 \tag{8}$$

3.2 Stress inversion using earthquake's FM

An alternative way to constrain S_H relies on the inversion of the FM solutions for the relative stress magnitudes represented by the shape factor *R* from Eqn (2) in combination with knowledge of the other two components of the stress tensor. This starts with the assumption that a fault slip is parallel to the shear traction force on the faulting plane [*Wallace*, 1951]; consequently, such slip directions obtained from observed earthquake FM solutions may be inverted for the relative deviatoric components of the stress tensor that may be used to construct the shape factor *R* (Eqn. 2).

The *R* obtained from FM is in a normalized form and by itself provides no indication of actual stress magnitudes. However, an examination of Eqn. 2 shows that if *R* and two of the principal stress magnitudes are known, then the third is easily calculated. Here, under the Andersonian stress state assumption in a strike-slip environment as indicated by the FM for the M_W 3.8 *Event A*, and with known $\sigma_2 = S_V$, and $\sigma_3 = S_h$, the maximum principal stress $\sigma_1 = S_H$ is readily calculated [e.g., *Hardebeck and Hauksson*, 2001]. Here, the single FM is available from this *Event A* (see **Table 1**) is used first to determine *R*, assuming it occurs in or near the Duvernay Formation; S_H may be calculated using the predicted S_V and S_h magnitudes.

One well-known complication, however, is that the FM solution for an arbitrary earthquake yields two possible conjugate slip planes: a true and an auxiliary fault plane; and without additional complementary geological observations, cannot be discriminated from one another. There are, however, numerous strategies that attempt to determine which plane may be preferred. We do not take such a direct approach here; instead, we invert the two possible conjugate planes from *Event A* to determine R and S_H as described above. This was accomplished using modified inversion subroutines from *Vavryčuk*'s [2014] recently published code to each of the conjugate planes in isolation. The distribution of possible R values (**Figure 7a**) was calculated in a 1000-realization Monte-Carlo approach; the orientation of each conjugate plane (see **Table 1**) randomly varied by up to ±5° to account for expected uncertainties in the FM solution.

Both solutions suggest an S_H azimuth ϕ of 45 º– 60 º, in agreement with our prediction through borehole observations. However, the axis of σ_2 (equivalent to S_V under the assumed Andersonian stress regime) deviates from vertical from ~18 - 40º (Figure S2). This potentially reflects the local stress concentration, which is not accounted for in this study and admittedly requires further analysis. Without considering uncertainty, direct stress inversion performed on both planes report similar shape ratios (0.621 for plane 1 and 0.608 for plane 2); adding ranges of uncertainty to the FM solution for *Event A* (**Table 1**) produces similar distributions of R between 0.55 and 0.67 (median 0.62, **Figure 7a**). Using the early constrained quantitative stress magnitudes of 40.3 MPa ≤ S_h ≤ 50.9 MPa and 58.0 MPa ≤ S_V ≤ 63.4 MPa together with the estimated range of values for R via rearrangement of Eqn. 2 allows for the range 65 MPa ≤ S_H ≤ 106 with median S_H = 84 MPa (see **Figure 7b**). Considering the uncertainties and caveats associated with this approach, the higher bounds of the uncertainty for S_h (5.3 MPa, see section

3.3) are used; the uncertainty of S_V (2.7 MPa) is selected from the regional average, given the abundant well logs used for the 3D density model (see Text S2 for details). Using stress inversion results from either conjugate plane does not change the distributions of S_H significantly. S_H constrained through this approach is consistent with that S_H of 75–116 MPa (see **Figure 6**) constrained from borehole failures.

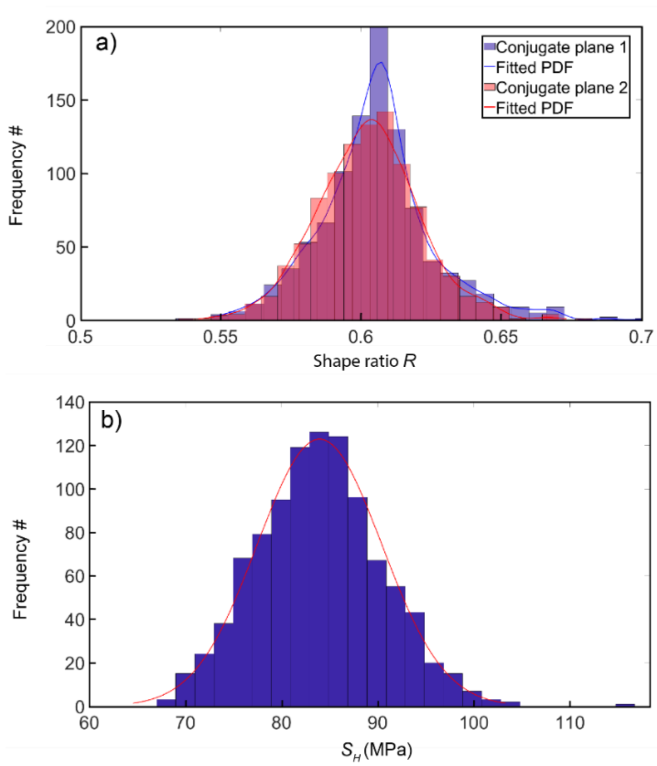

Figure 7. a) The distribution of shape factor *R* computed for both conjugate fault planes from the earthquake's (M_W 3.8/M_L 4.2) focal mechanism solution, and **b)** inverted S_H with the predicted S_h and S_V at the epicenter, using the *R* distribution from conjugate plane 1, assuming an Andersonian strike-slip stress regime.

3.3 A predictive stress model

Similar to a previous study in the Fox Creek area to the north [*Shen et al.*, 2019a], we provide a Matlab™ program (RD_stress.m, see supporting information/data for details), allowing users to estimate the stress magnitudes within the Duvernay Formation beneath the desired surface position in the study area. This program assumes the tangent gradients of S_h and P_P can be confined by the ranges of the slopes computed through linear regression (Eqn. 3 and 4). As such, at depths reasonably close to the Duvernay, the magnitudes of S_h and P_P are estimated by interpolating for the values at the surface of the Duvernay Formation (**Figure 4e** and **g**). Subsequently, the obtained stress values are shifted to the depth of interest with the respective tangent gradients. Uncertainties (**Figure 4f** and **h**) are calculated from the errors (**Figure 5a** and **b**) and the ranges of the slopes constrained from linear regression (see Eqn. 3 and 4). The same approach is adapted for S_V, with the tangent gradient assumed to be between 25 and 27 kPa/m (derived from the densities of the Duvernay rocks assuming a constant gravity acceleration of 9.8 m/s^2). In this study, we only constructed a 2D stress-orientation map due to the lack of observed depth dependency. In summary, through simple cubic interpolation of results, the program reports the orientation of the stress tensor and our relative prediction confidence for any given map location.

Spatial maps for S_h (**Figure 4e**) and P_P (**Figure 4g**) are constructed through the methods that had been discussed in *Shen et al.*, [2018; 2019a]. Briefly speaking, each measurement is shifted to the top of the Duvernay with the tangent gradient $\Delta S_h(z)/\Delta z$ and $\Delta P_P(z)/\Delta z$ calculated through linear regression (Eqn. 3 and 4). Simple Kriging is subsequently performed with uncertainties (from original observation and linear regression) accounted – the square root of kriging variance provides an assessment to the uncertainties of our final maps. At sufficient distance, the prediction essentially becomes the average value of all observations. In our model, the uncertainties of S_h and P_P near observations generally range from 0.5 MPa to 1 MPa and rises to as high as 5.5 MPa for S_h and 5 MPa for P_P at distances further away. Generally, we consider the values predicted within the white contours in **Figure 4e - g** to be reliable, which mark the uncertainties of 5 MPa for S_h and 4.5 MPa for P_P.

4 Discussion

4.1 Comparison of S_h and P_P with Fox Creek area.

An early motivation for this study was to determine whether there are any substantive differences in the stress states in the Fox Creek region that had displayed significant induced seismicity to the current study area, which is largely aseismic. In both areas, at the depth of the Duvernay Formation, a strike-slip faulting regime is indicated by the observed $S_V > S_h$ and FM. The secant gradients do not show significant variation between the two areas (**Table 2**). In contrast, however, some differences appear in the tangent gradients with that for the Fox Creek (32.1 ± 3.1 MPa/km) exceeding that for the current Red Deer Study area (22.2 ± 5.6 MPa/km). However, some care must be taken before making a general interpretation as some geographic complications between the West Shale Basin and East Shale Basin. The five S_h values from the East Shale Basin, all at shallower depths from 2157 m to 2331 m, bias the aggregate slope. Repeating the regression using only the Williston Green values from 2300 m to 3500 m gives an S_h tangent gradient that agrees with that for the Fox Creek area - the reasons for this are not known. The Fox Creek and Willesden Green zones, although more than 200 km from each other, both lie within the West Shale Basin and may have similar behavior. Alternatively, this may be due to differences in the depths at which the measurements are made.

The tangent slopes for the P_P appear lower over the current study area relative to the Fox Creek zone. However, there remains a great deal of scatter in the measured values (**Figure 5b**), and within the uncertainty, both slopes are similar.

Taken together, there does not appear to be significant differences in the S_h and P_P trends between the two zones, although there are indications that the observed values of S_h within the East Shale Basin are elevated relative to the predicted trend (Eqn. 3). It is important to note that the stress model, which relies on kriging of the observed values, retains these local variations. However, it does not appear that the regional differences in S_h and P_p could explain the variations in levels of seismicity between the Fox Creek region and the current study areas.

Table 2. Comparison of calculated stress and pore pressure gradients between the Fox Creek and Red Deer study areas.

Area	Gradient type (see text for details)	Red Deer (MPa/km)			Fox Creek (MPa/km)
		Mesozoic	Duvernay Aggregate	Duvernay Willesden Green Only	Duvernay
Range of Measurement Depths (km)		1.3-3.0	2.1-3.5	2.3-3.5	2.9-3.9
S_V	Secant		24.5 ± 0.5		24.5 ± 1.0
S_h	Secant	16.8 ±3.2	18.3 ± 3.6	18.0 ± 3.3	19.2 ± 2.8
	Tangent	19.1 ± 2.4	22.2 ± 5.6	34.2 ± 6.0	32.1 ± 3.1
P_P	tangent		24.8 ± 3.6		29.1±7.2

4.2 Relation to other seismicities in the area

It is useful to contrast this situation with that in the nearby RMHSZ (near 52'12.5'N. 115'15'W), which lies within the deformation belt and where, as noted earlier, events were likely associated with sour gas production from Leduc Formation reefs through the 1980s. The foci of these events are reported at depths around 5.2 km (3.2 kmbsl) [*Wetmiller*, 1986], with a modest M_W 3.4 (*Event C)*; the FM solution indicates this earthquake happens on an oblique reverse fault contrasting with the primarily strike-slip FM for *Event A.*

Using nearby measurements from boreholes compiled by *McLellan* [1989], *Baranova et al.* [1999] provided estimates for the Andersonian stress magnitudes at the depth of *Event C's* focus obtaining relative $S_V < S_h < S_H$ - an observation that disagrees with our model, which predicts, at this location, a significantly larger S_V such that $S_h < S_V < S_H$. One component of this discrepancy appears to be due to confusion in the use of elevations in *Baranova et al.* [1999] instead of the correct depths reported by *McLellan* [1989], which differ by more than 1 km - as such, their stress model appears to have inadvertently underestimated the S_V magnitudes. Regardless, our observed strike-slip stress state is less consistent with the largely reverse faulting mechanism FM for *Event C*; this may indicate that the stress regime within the disturbed belt differs from that outside of it.

4.3 Stability analysis for the M_W 3.8 earthquake (Event A)

We assess the ranges of fault *SNR* at *Event A's* focus by calculating the normal σ and shear τ tractions resolved onto all possible planes [*Shen et al.* 2019b] using the stress model's predicted stress states (**Table 1**) with the most probable S_H magnitude (84 MPa). The calculations were repeated with three different P_f of i) absent $P_f = 0$ (**Figure 8a**), ii) $P_f = P_H$ of the normal hydrostatic pressure assuming a standard water pressure gradient of 10 MPa/km

(**Figure 8b**), and iii) $P_f = P_P$ (**Figure 8c**) as found in our model interpolated from the transient borehole fluid tests in the Duvernay Formation. A previous meta-analysis of laboratory frictional measurements [*Shen et al.*, 2019b] suggested friction ranged $0.4 < \mu < 0.8$; these bounding values are shown for the sake of reference as contours in **Figure 8**. Although we do not know the actual frictional coefficients acting at *Event A*'s focus, this is taken to be a reasonable range to assess stability. For example, one might expect that those planes subject to $SNR < 0.4$ will remain clamped while those with $SNR > 0.8$ will be increasingly prone to slip. As such, **Figure 8** demonstrates how P_f controls fault stability.

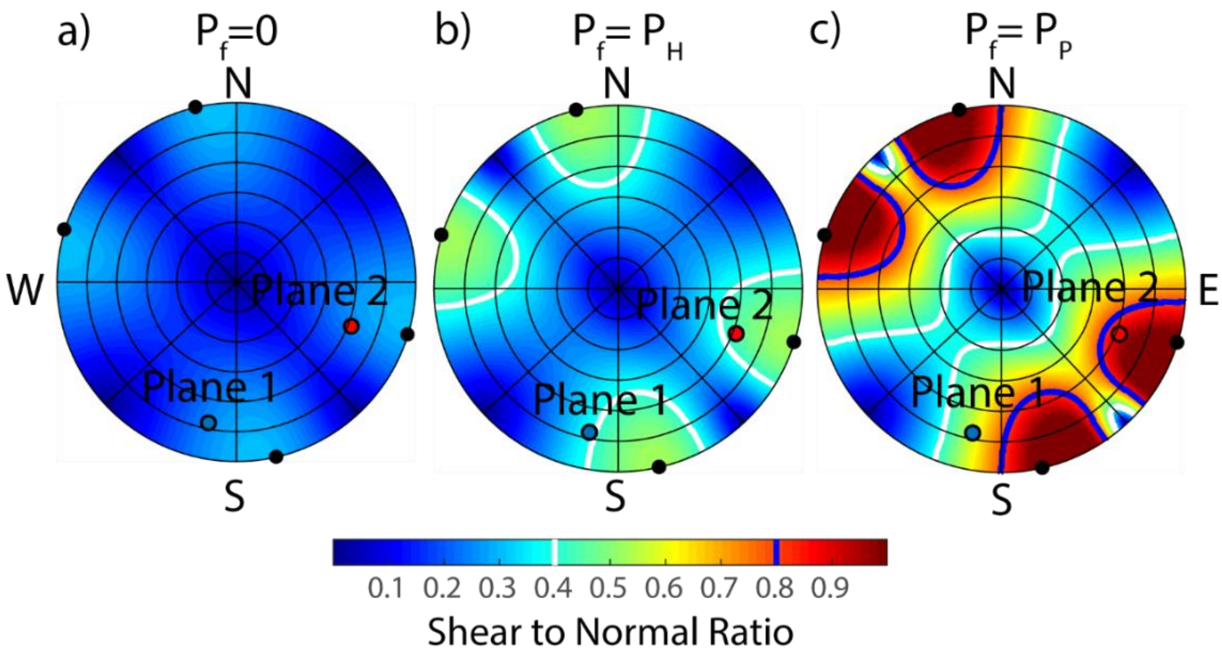

Figure 8. Stereonets of the *SNR* on all possible planes at *Event A's* focus calculated assuming vanishing cohesion *C* with a) no fluid pressure $P_f = 0$, b) normal hydrostatic pressure $P_f = P_H$, and c) Duvernay Formation pore pressure $P_f = P_P$. Blue and red dots are the poles of the two conjugate planes of the event's FM. Black dots indicate the poles for hypothetical optimally oriented planes. Blue and white contours delineate $SNR = 0.8$ and 0.4.

Examination of **Figure 8a**, **b** suggests that if $P_f \leq P_H$ both conjugate planes are likely to remain clamped (i.e., *SNR* < 0.4). *Eyre et al.* [2019], for example, in their study near Fox Creek, presume that $P_f = P_H$ within the Duvernay Formation and estimate *SNR* ~ 0.29; they suggest this would preclude active seismic slip. However, if P_f is at the expected ambient formation pore pressure P_P as provided in this study, both conjugate planes are significantly destabilized with the *SNR* for Plane 2, which strikes at 201°, falling outside the *SNR* = 0.8 contour (**Figure 8c**).

One final point arising from **Figure 8** is that both of the possible conjugate planes do not match those that are optimally oriented for slip (i.e., 30° from S_H azimuth, assuming $\mu = 0.6$) within the stress field. These results are similar to the conclusions of *Shen et al.* [2019b] for eleven events in the Fox Creek area and a number of the events induced by long-term injection near Prague, OK [*Cochran et al.*, 2020].

4.4 *Areal constraints on stability*

The stereographic projections of **Figure 8** show only three specific stress regimes but include uncertainties of the pressures and frictions. This allows for a broader range of possible stability conditions and more stochastic analysis – an approach that is now widely employed to assess the risk of seismicity through various derived metrics [e.g., *Seithel et al.*, 2019; *Shen et al.*, 2019b; *Walsh and Zoback*, 2016; *Yaghoubi et al.*, 2020]. To better explore these relationships, the critical values of P_f^c required to induce slip [e.g., *Mukuhira et al.*, 2017; *Streit and Hillis*, 2004]

$$P_f^c = \frac{\mu\sigma - \tau + C}{\mu} \tag{8}$$

were calculated separately on each of Event A′s conjugate planes in a Monte Carlo simulation with 5000 *SNR* realizations that used values of friction $0.4 < \mu < 0.8$, of cohesion $0 < C < 5$ MPa, and ranges of the three principal stresses (**Table 1**). These realizations also accounted for uncertainties of the plane's strikes, dips, and rakes by varying these angles randomly by ±5° with the resulting distributions of the shear τ (**Figure 9a**) and normal (clamping) σ (**Figure 10b**) tractions shown. The σ distribution on Plane 2 is lower and distinct from that of Plane 1, suggesting that Plane 2 is more readily movable.

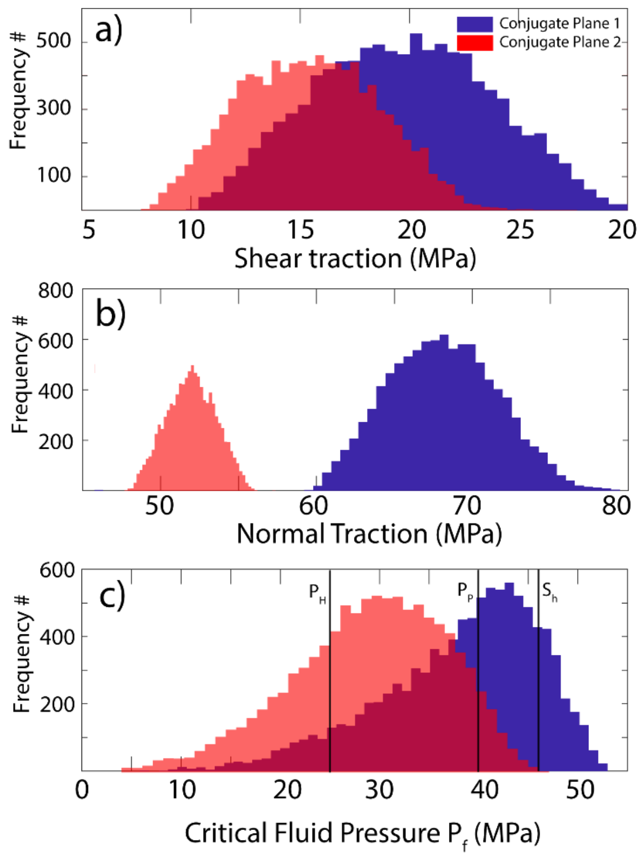

Figure 9. Monte Carlo distributions of **a)** shear traction, **b)** normal clamping traction and **c)** critical P_f^c required for slip on either *of Event A's* conjugate planes.

The corresponding critical P_f^c distributions (**Figure 9c**), too, differ significantly. Both distributions are asymmetric, and their peaks are offset. Plane 2's distribution shifted to significantly lower pressures indicating that, again, Plane 2 may more easily slip. The most vulnerable plane is often presumed to be that actually responsible for the earthquake [e.g., *Alt and Zoback*, 2016; *Vavryčuk*, 2014]. This may suggest, but cannot prove, that *Event A* occurred on Plane 2; both distributions have long tails to low $P_{f,}$ offering a, though improbable, possibility that slip could be triggered on Plane 2 by pressures as low as 4 MPa. It is useful to examine **Figure 9c** for some typical values of P_f. Significant fractions of both distributions lie below that expected for the normal hydrostatic gradient $P_f = P_{H,}$ further indicating that slip could initiate even for relatively low fluid pressures.

More interestingly, the Duvernay Formation reservoir at P_P is highly overpressured [*Cochran et al.*, 2020; *Eaton and Schultz,* 2018; *Shen et al.*, 2019b - more than 90% of Plane 2's distribution lies below this P_P. This means that there is a high likelihood of it being unstable, particularly if the fluid pressures are of those expected in the reservoir. About 50% of the situations available to Plane 1, in contrast, also lie below this pressure. This is the same situation, although shown through a more statistical analysis here, as that encountered to the north in the Fox Creek area [*Shen et al.*, 2019b] where the faults were expected to be unstable at the natural pore pressure; the lack of natural, historical seismicity in the area suggests that the fluid pressure acting along the planes of weakness are likely lower. The Plane 2 distribution in **Figure 9c** does admit stable cases when $P_f = P_{P,}$ but this is not likely. In contrast, about 50% of the cases for Plane 1 remain stable for this condition.

It is also useful to compare the case of $P_f = S_h$. This pressure is a useful reference because S_h determined from the pressure at which the fracture, artificially created during a transient pressure test and whose plane is presumed to be perpendicular to the S_h direction, is deemed to close (see review in *Schmitt and Haimson* [2017]). As such, it provides a lower bound to the fluid pressures transmitted into the formation along an artificial fracture and, subsequently, to the fault should a direct hydraulic connection be established. The peaks for both distributions, and indeed the entire distribution for Plane 2, falls below $S_{h,}$ indicating that fluid pressures this high would certainly destabilize the fault.

In summary, two points are raised by the analysis of the critical P_f^c distributions in **Figure 9c**. First, the natural reservoir pressure P_P alone is sufficient to destabilize a relatively wide range of appropriately oriented planes of weakness; and the question arises as to why the more natural seismic activity is not present. And second, production-based HF operations at this site that must extend fluid pressures, which must exceed S_h to propagate fractures, will readily provide sufficient critical P_f to induce slip on both on both of the FM's conjugate planes; this is similar to that from the Fox Creek area [*Shen et al.*, 2019b; *Yaghoubi et al.*, 2020].

These observations are reinforced in more direct comparative examinations of *SNR* as a function of P_f for both conjugate planes along with a hypothetical fault plane optimally oriented to the stress field (i.e., 30° from S_H azimuth, assuming μ = 0.6). These results are displayed in **Figure 10**, which is intended to compare the critical P_f^c to fault stabilities. The red and green ribbons represent envelopes for the set of the *SNR* calculations that, respectively, assume cohesions of either $C = 0$ or C = 5 MPa used in the construction of **Figure 9c**. The green ribbon in **Figure 10a**, for example, encompasses possible values of S_H constrained with both borehole failures and FM inversion; a maximum cohesion of 5 MPa is also employed. This envelope is superimposed on a gray background that simply highlights the likely range of friction coefficients $0.4 < \mu < 0.8$ to illustrate the P_f for which $SNR > \mu$ such that the fault is most likely to be unstable. As such, the portions of the envelopes above *SNR* = 0.8 and below *SNR* = 0.4

respectively delineate conditions under which the faults are highly likely to be either unstable or stable.

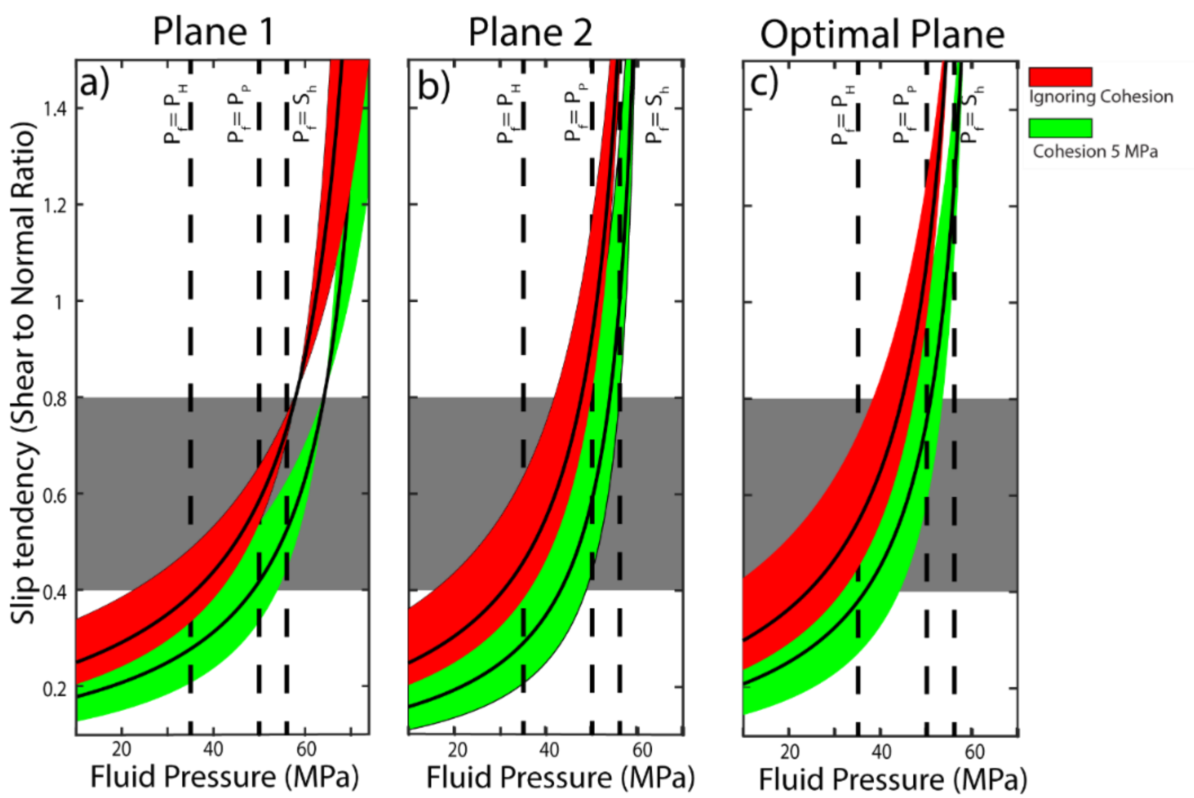

Figure 10. The slip tendency of the **a)** conjugate faulting plane 1, **b)** 2 of the FM solutions for the *Event A* (see **Table 1**), and **c)** a hypothetical fault oriented optimally (assuming μ = 0.6) for slip initiation. Red and green stripes represent the range of values calculated for the constrained bounds of S_H (75 – 106 MPa, median 84 MPa) account for either C (cohesion, see Eqn. 1) = 0, or 5 MPa. The grey box denotes the expected range of μ between 0.4 and 0.8.

4.5 Correspondence of seismicity and estimated susceptibility

In addition to assessing the stability of the induced event's fault planes, it is useful to further extend the stress model by using it to evaluate the susceptibility for induced seismicity more regionally. Following from **Figure 10**, we use the deviation of the critical fluid pressure P_f^c on the fault plane from the expected ambient $P_P(x,y)$:

$$\Delta P(x,y) = P_P(x,y) - P_f^c(x,y) \tag{9}$$

Although the choice of P_P is somewhat arbitrary, given its general trend with depth (see **Figure 5**), this measure does remove complications due to the variable Duvernay Formation depths while indicating how the level of pore fluid pressure perturbation necessary to induced slip. Progressively lower values of $\Delta P < 0$ indicates instability. Calculation of the fault's slip-tendency relies on the estimated value of P_f^c that in turn, requires knowledge of the fault's orientation. *Schwab et al.* [2017] and *Stork et al.* [2018] provide examples of studies that estimate the stability on actual faults or lineaments imaged in 3D reflection seismic volumes but other studies have used seismicity to outline fault trends [e.g., *Eyre et al.*, 2019; *Jia*, 2019]. To overcome this limitation, here, we carry out the calculations over the study area by first assuming that at each mapped point planes of weakness have the same orientation as the most stable Plane 1 (**Figure 11**, for Plane 2 the readers are referred to Figure S3) for *Event A* and then, second, for the sake of comparison, with the orientation planes optimally oriented to slip. For each orientation, the critical fluid pressure P_f^c is first calculated (**Figure 11a** and **b**) followed by ΔP (**Figure 11c** and **d**) in which the lower the value of ΔP, the greater the susceptibility. Though our earlier slip-tendency analysis suggests faults are unlikely to be oriented in these directions, this analysis does allow for a relative comparison.

We note that many authors instead employ Coulomb failure stress [e.g., *King et al.*, 1994]. We avoid this measure because it necessitates calculation of $\Delta\sigma$ and $\Delta\tau$ that in turn requires specific knowledge of the perturbing load and its geometry relative to the vulnerable fault plane [*Catalli et al.*, 2013], information that we do not at this time have. These can often be small, too, relative to the changes in P_f due to injection [e.g., *Segall*, 1985].

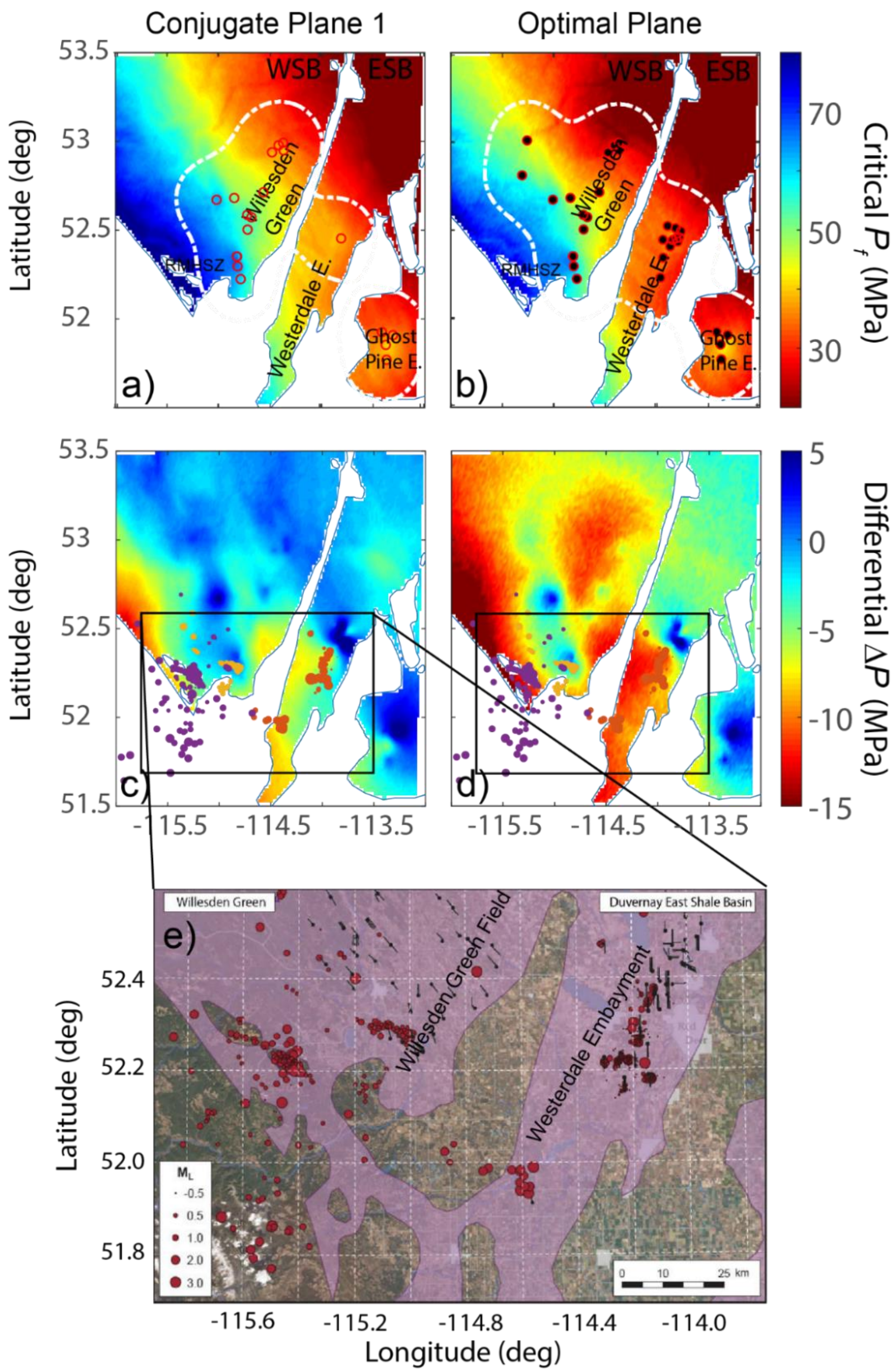

Figure 11. Required critical pressure P_f^c to activate hypothetical faults across the study area for **a)** hypothetical faults across the region oriented parallel to the conjugate plane 1 for the Red Deer earthquake listed in Table 1, and **b)** assumed faults oriented optimally to slip. **c)** and **d)** are the corresponding pressure difference ΔP (= P_f^c - P_P) shown in a) and b). Brown, orange, and purple dots are the induced earthquake clusters in ESB, WG, and RMHSZ, respectively. Empty red circles denote the locations of S_h measurements, and solid circles represent that of P_P measurements. **e)** The study area in *Schultz and Wang* [2020], with earthquake locations and nearby HF wells.

Both sets of ΔP maps (**Figure 11c** and **d**) are mostly similar within the Westerdale Embayment's southern portion, displaying high values. In contrast, the immediately adjacent northern portions of the Westerdale Embayment and the Ghost Pine Embayment have positive ΔP indicating suggesting that these zones are relatively more stable. This observation may help to explain the clusters of induced events within the south Westerdale Embayment (see **Figure 12c - e**) and their absence in the Ghost Pine Embayment and north Westerdale Embayment despite significant hydraulic fracturing activity there (**Figure 11e**).

The good correlation between the ΔP susceptibility and seismicity just described is not as successful in the Willesden Green Field in the West Shale Basin immediately to the north on the other side of the Rimbey-Meadowbrook Reef Trend. Although the ΔP (**Figure 11c - d**) there is generally high, the Duvernay Formation seismicity observed in this area (orange dots) occurs within an area, though of only lower magnitudes (M_W < 2, *Schultz and Wang*, [2020]), that on the basis of ΔP, appears relatively more stable. This conflicts with the lack of events immediately to the east, where significantly less stable ΔP are seen regardless of the significant hydraulic fracturing activities.

There are several possible reasons for this discrepancy. First, to have an induced event, one presupposes the existence of an appropriate plane of weakness upon which sliding may occur. The aseismic zones may simply not have any vulnerable structures upon which sliding might occur. It may also be that such vulnerable structures do exist in these areas, but none of the hydraulic fracturing operations were within range to attain hydraulic connection [*Wilson et al.*, 2018]. Second, the stress and pore pressure model may not accurately predict the conditions everywhere within the study area. While we are generally confident in the results that lie within the white boundaries in **Figures 4** and **11**, there are some areas with fewer or no measurements that the extrapolations may not be valid due to geological complexity. This problem is particularly severe for S_H - the values for which were not directly measured but constrained with a rather broader uncertainty. A third possibility is that vulnerable planes of weakness do exist, but stresses may have already been relieved by events prior to the historical record, aseismically, or via many smaller events that are not observed or cataloged.

As such, the relative susceptibility mapping of **Figure 11** should not, without further information, be interpreted directly to indicate zones where induced earthquakes will/would occur, but rather provide additional constraints on the risks associated with a given perturbation in pressure. It would be useful to build on this model by comparing it against actual hydraulic fracturing pressure records. More specifically, how do the actual pressures attained during hydraulic fracture stimulations compare to the estimated P_f^c? Might the pressures employed in the aseismic eastern portion of the Willesden Green Field be lower than those used near the cluster of seismicity? Addressing these questions is beyond the scope of the current study; it is unknown whether the appropriate data even exists or could be accessed, but carrying out such an examination would test the validity of this stability analysis.

4.6 What factors control the induced seismicity

That human activities might initiate earthquakes has been known since the middle of the last century with a great deal of interest on earthquakes stimulated by deep fluid waste injections of the Denver earthquakes [e.g., *Healy et al.*, 1968], from crustal loading of large surface hydroelectric reservoirs [e.g., *Gough and Gough*, 1970; *Gupta*, 2018], due to stimulation and operation of geothermal reservoirs [e.g., *Zang et al.*, 2014], hydrocarbon energy production [e.g., *Suckale*, 2009; *Wetmiller*, 1986], long term disposal of water or greenhouse gases [e.g., *Ellsworth*, 2013] and hydraulic fracture stimulation [e.g., *Atkinson et al.*, 2016; *Fasola et al.*, 2019; *R Schultz et al.*, 2020].

An extensive literature supplying hypotheses have been developed to explain the mechanisms causing such induced earthquake; but virtually all of these require that the effective state of stress resolved on the vulnerable fault plane be sufficiently perturbed that Mohr-Coulomb frictional resistance, whether it be a static value or a derived from a time-dependent rate-state model. This may be accomplished by either or both of locally modifying the state of total stress from the imposition of the new load nearby or by reducing the effective compressive traction normal traction σ by increasing the fluid pressure P_f [e.g., *Garagash and Germanovich*, 2012]. Recent experimental investigations also suggested that the effective initial stress also controls the rupture velocities and, thus, the earthquake types (i.e., seismic or aseismic; [*Passelègue et al.*, 2020]). Studies attempting to explain the responsible mechanism usually focus on one or the other as being primarily responsible, but changes in both should be expected to contribute to greater or lesser extents.

Different types of perturbing loads have been invoked. Some studies employ analytic elastic dislocation solutions [e.g., *Green and Sneddon*, 1950; *Pollard and Segall*, 1987; *Warpinski*, 2000] to calculate the stress field generated by a fluid-filled hydraulic fracture that is superposed to the existing stress field resolved onto a fracture plane [e.g., *Kettlety et al.*, 2020]. Other models have calculated the perturbing stresses using poroelastic analytic [e.g., *Baranova et al.*, 1999; *Goebel et al.*, 2017; *Segall*, 1985; *Segall and Lu*, 2015], or numerical [e.g., *Cueto-Felgueroso et al.*, 2018; *Deng et al.*, 2016] solutions. Depending on the availability of fluid pathways in the reservoir, fluid pressures changes due to fluid diffusion, too, are important [e.g., *Shapiro and Dinske*, 2009] and may explain some delays in seismicity in some cases [e.g., *Baisch et al.*, 2010].

Our fault stability analyses here show that the active fluid pressure P_f is likely the most crucial factor, given that the expected natural pore pressures are already at ~90% of S_h. This indicates that even before anthropogenic disruption, the slip surface for *Event* A was already critically loaded. Consequently, the problem in trying to target the mechanisms ultimately responsible for triggering the slip, in this case, is that only small perturbations in σ, τ, and P_f might be required; this confounds clear discrimination of which factors are most important. Though various scenarios that might favor one or the other mechanisms can be modeled, during an HF stimulation, fluid pressures that often significantly in excess of S_h are introduced to the system [e.g., *Kleiner and Aniekwe*, 2019]. The low matrix permeabilities of the rocks within and surrounding the Duvernay Formation, and many other unconventional shale oil/gas reservoirs, likely preclude diffusive fluid pressure transfers - fluid pressures need to be transmitted via more transmissive natural fractures systems [*Lele et al.*, 2017; *MacKay et al.*, 2018]. In contrast, induced poroelastic changes from a fracture are relatively modest in comparison [*Baranova et al.*, 1999; *Deng et al.*, 2016; *Goebel et al.*, 2017], suggesting that direct hydraulic connectivity may be the most important component in these cases [*Lele et al.*, 2017].

5 Conclusions

The current study area had, on the basis of the lack of seismicity, been assessed to have low seismic risk. Recent earthquakes that are related to hydraulic fracturing operations motivate further analysis. A more deterministic analysis that includes a geomechanical evaluation of fault slip-tendency is required to assist in explaining both the prior lack of seismicity and the recent events.

We developed a quantitative 3D model that estimates the Andersonian stress tensor (S_H, S_h, S_V, and ϕ) from borehole logs and transient pressure tests. This model incorporated information from both borehole breakouts and inversion of the limited focal mechanism solution available to provide ranges of S_H's magnitudes. Despite the large uncertainties, an agreement is reached between the two methods, and our best estimation of S_H falls between 75 MPa and 106 MPa at the epicenter of the M_W 3.8/M_L 4.2 (Red Deer, Alberta) earthquake.

We extended this model to further study the mechanical stability of the two possible conjugate fault planes associated with the Red Deer earthquake (M_W 3.8). Both planes would remain stable if the fluid pressure acting on the fault P_f is at the normal hydrostat. However, both are expected to be naturally unstable if P_f is the same as the nominal pore fluid pressure P_P measured from boreholes in the target Duvernay Formation. The historical lack of seismicity in the area may suggest that the high natural P_P can only be dissipated on the faults, perhaps by leakage to overlying Mesozoic formations. Further, neither of the possible conjugate planes are optimally oriented to the stress field - a range of other planes of weakness are more susceptible to slippage. These findings suggest that the induced seismicity is triggered by elevating the fluid pressures on the fault via direct fluid pathways from the hydraulic fracture operations.

Motivated by such findings, we subsequently performed susceptibility analysis for the study area using both the critical P_f^c needed to activate a fault and its difference to the expected ambient P_P ($\Delta P = P_f^c - P_P$) as metrics. These suggest that the Ghost Pine Embayment to the southeast and the North Westerdale Embayment are generally stable (requires $P_f^c > P_P$ to be activated). This finding agrees with the general absence of earthquakes reported from seismological observations. The high-profile Red Deer M_W 3.8/M_L 4.2 earthquake happened in a zone we considered to be less stable owing to the high P_P modeled with transient wellbore fluid tests.

Before concluding, it is worthwhile to reinforce that our analysis, both the stereographic projections analysis (see **Figure 9**) and the susceptibility maps (see **Figure 12**) are derived solely from the stress tensor. These analyses are not influenced by the study areas' past earthquake records or seismic quiescence that might be biased by the industry activities or regional seismometer station network's detection limit [*R Schultz et al.*, 2015] – a fresh perspective on controlling factors of HF induced seismicity and seismic susceptibilities are provided here.

Acknowledgments, Samples, and Data

L. W. Shen and T. E. Hauck's contributions to this work are supported by the Alberta Energy Regulator (AER). Mahshid Babakhani is thanked for providing the model cross-section image in **Figure 1**. Earlier components of D. R. Schmitt's contribution are supported by the NSERC at the University of Alberta and currently through the Stephen and Karen Brand Professor and Purdue University. Supplementary data includes the transient well testing results, borehole image log analysis results, Matlab™ program RD_stress are accessible through the Mendeley data repository at **https://data.mendeley.com/datasets/tgmxx5vkjx/1**

References

Alberta Energy Regulator (AER, 2015), Subsurface order no. 2: Monitoring and reporting of seismicity in the vicinity of hydraulic fracturing operations in the Duvernay zone, Fox

Creek, Alberta, *[Available at http://www.aer.ca/documents/bulletins/Bulletin-2015-07.pdf]. 3 pages*.

Alberta Energy Regulator (AER, 2019), Subsurface Order No. 7, *[Available at https://static.aer.ca/prd/documents/orders/subsurface-orders/SO7.pdf]. 4 pages*.

Alt, R. C., and M. D. Zoback (2016), In situ stress and active faulting in Oklahoma, *Bull. Seismol. Soc. Amer.*, *107*(1), 216-228.

Anderson, E. M. (1951), *The dynamics of faulting and dyke formation with applications to Britain*, Oliver and Boyd.

Atkinson, G. M., D. W. Eaton, H. Ghofrani, D. Walker, B. Cheadle, R. Schultz, R. Shcherbakov, K. Tiampo, J. Gu, and R. M. Harrington (2016), Hydraulic fracturing and seismicity in the Western Canada Sedimentary Basin, *Seismological Research Letters*, *87*(3), 631-647.

Baisch, S., R. Vörös, E. Rothert, H. Stang, R. Jung, and R. Schellschmidt (2010), A numerical model for fluid injection induced seismicity at Soultz-sous-Forêts, *International Journal of Rock Mechanics and Mining Sciences*, *47*(3), 405-413.

Baranova, V., A. Mustaqeem, and S. Bell (1999), A model for induced seismicity caused by hydrocarbon production in the Western Canada Sedimentary Basin, *Canadian Journal of Earth Sciences*, *36*(1), 47-64.

Barton, C. A., M. D. Zoback, and K. L. Burns (1988), In-situ stress orientation and magnitude at the Fenton Geothermal Site, New Mexico, determined from wellbore breakouts, *Geophysical Research Letters*, *15*(5), 467-470.

Beaumont, C. (1981), Foreland basins, *Geophysical Journal International*, *65*(2), 291-329.

Bell, J., and S. Bachu (2003), In situ stress magnitude and orientation estimates for Cretaceous coal-bearing strata beneath the plains area of central and southern Alberta, *Bulletin of Canadian Petroleum Geology*, *51*(1), 1-28.

Bell, J., and G. Caillet (1994), A reinterpretation of the stress regime of the Aquitaine basin, southwestern France, and implications for hydrocarbon recovery, in *Hydrocarbon and Petroleum Geology of France*, edited, pp. 209-219, Springer.

Bell, J., and D. Gough (1979), Northeast-southwest compressive stress in Alberta evidence from oil wells, *Earth and planetary science letters*, *45*(2), 475-482.

Bell, J., and S. Grasby (2012), The stress regime of the Western Canadian sedimentary basin, *Geofluids*, *12*(2), 150-165.

Bank of Montreal (BMO, 2019), East of the reef - Duvernay Oil Play, in *BMO Capital Markets - Energy - A & D Advisory*, edited.

Bott, M. H. P. (1959), The mechanics of oblique slip faulting, *Geological Magazine*, *96*(2), 109-117.

Bouzidi, Y., D. R. Schmitt, R. A. Burwash, and E. R. Kanasewich (2002), Depth migration of deep seismic reflection profiles: crustal thickness variations in Alberta, *Canadian Journal of Earth Sciences*, *39*(3), 331-350.

Burwash, R., C. McGregor, and J. Wilson (1994), Precambrian Basement Beneath the Western Canada Sedimentary Basin, Geological Atlas of the Western Canada sedimentary Basin, 49-56, *Alberta Research Council*.

Castaños, H., and C. Lomnitz (2002), PSHA: Is it science?, *Engineering Geology*, *66*(3-4), 315-317.

Catalli, F., M. A. Meier, and S. Wiemer (2013), The role of Coulomb stress changes for injection-induced seismicity: The Basel enhanced geothermal system, *Geophysical Research Letters*, *40*(1), 72-77.

Chen, Y., Y. J. Gu, C. A. Currie, S. T. Johnston, S.-H. Hung, A. J. Schaeffer, and P. Audet (2019), Seismic evidence for a mantle suture and implications for the origin of the Canadian Cordillera, *Nature communications*, *10*(1), 1-10.

Chopra, S., R. K. Sharma, A. K. Ray, H. Nemati, R. Morin, B. Schulte, and D. D'Amico (2017), Seismic reservoir characterization of Duvernay shale with quantitative interpretation and induced seismicity considerations—A case study, *Interpretation*, *5*(2), T185-T197.

Cochran, E. S., R. J. Skoumal, D. McPhillips, Z. E. Ross, and K. M. Keranen (2020), Activation of optimally and unfavourably oriented faults in a uniform local stress field during the 2011 Prague, Oklahoma, sequence, *Geophysical Journal International*, *222*(1), 153-168.

Corlett, H., R. Schultz, P. Branscombe, T. Hauck, K. Haug, K. MacCormack, and T. Shipman (2018), Subsurface faults inferred from reflection seismic, earthquakes, and sedimentological relationships: Implications for induced seismicity in Alberta, Canada, *Mar. Pet. Geol.*, *93*, 135-144.

Cueto-Felgueroso, L., C. Vila, D. Santillán, and J. C. Mosquera (2018), Numerical Modeling of Injection-Induced Earthquakes Using Laboratory-Derived Friction Laws, *Water Resources Research*, *54*(12), 9833-9859.

Deng, K., Y. Liu, and R. M. Harrington (2016), Poroelastic stress triggering of the December 2013 Crooked Lake, Alberta, induced seismicity sequence, *Geophysical Research Letters*, *43*(16), 8482-8491.

Eaton, D. W., N. Igonin, A. Poulin, R. Weir, H. Zhang, S. Pellegrino, and G. Rodriguez (2018), Induced Seismicity Characterization during Hydraulic-Fracture Monitoring with a Shallow-Wellbore Geophone Array and Broadband Sensors, *Seismological Research Letters*, *89*(5), 1641-1651.

Eaton, D. W., and R. Schultz (2018), Increased likelihood of induced seismicity in highly overpressured shale formations, *Geophysical Journal International*, *214*(1), 751-757.

Eberhart-Phillips, D., and D. H. Oppenheimer (1984), Induced seismicity in The Geysers geothermal area, California, *Journal of Geophysical Research: Solid Earth*, *89*(B2), 1191-1207.

Edwards, D. J., and R. J. Brown (1999), Understanding the influence of Precambrian crystalline basement on Upper Devonian carbonates in central Alberta from a geophysical perspective, *Bulletin of Canadian Petroleum Geology*, *47*(4), 412-438.

Ekpo, E., D. Eaton, and R. Weir (2017), Basement Tectonics and Fault Reactivation in Alberta Based on Seismic and Potential Field Data, in *Geophysics*, edited, IntechOpen.

Ellsworth, W. L. (2013), Injection-induced earthquakes, *Science*, *341*(6142), 1225942.

Eyre, T. S., D. W. Eaton, M. Zecevic, D. D'Amico, and D. Kolos (2019), Microseismicity reveals fault activation before M w 4.1 hydraulic-fracturing induced earthquake, *Geophysical Journal International*, *218*(1), 534-546.

Fasola, S. L., M. R. Brudzinski, R. J. Skoumal, T. Langenkamp, B. S. Currie, and K. J. Smart (2019), Hydraulic fracture injection strategy influences the probability of earthquakes in the Eagle Ford shale play of South Texas, *Geophysical Research Letters*, *46*(22), 12958-12967.

Frankel, A. (2013), Comment on "Why earthquake hazard maps often fail and what to do about it" by S. Stein, R. Geller, and M. Liu, *Tectonophysics*, *592*, 200-206.

Galloway, E., T. Hauck, H. Corlett, D. Pană, and R. Schultz (2018), Faults and associated karst collapse suggest conduits for fluid flow that influence hydraulic fracturing-induced seismicity, *Proceedings of the National Academy of Sciences*, *115*(43), E10003-E10012.

Garagash, D. I., and L. N. Germanovich (2012), Nucleation and arrest of dynamic slip on a pressurized fault, *Journal of Geophysical Research: Solid Earth*, *117*(B10).

Goebel, T., M. Weingarten, X. Chen, J. Haffener, and E. Brodsky (2017), The 2016 Mw5. 1 Fairview, Oklahoma earthquakes: Evidence for long-range poroelastic triggering at> 40 km from fluid disposal wells, *Earth and Planetary Science Letters*, *472*, 50-61.

Gough, D., and W. Gough (1970), Load-induced earthquakes at Lake Kariba—II, *Geophysical Journal International*, *21*(1), 79-101.

Green, A., and I. Sneddon (1950), The distribution of stress in the neighbourhood of a flat elliptical crack in an elastic solid, paper presented at Mathematical Proceedings of the Cambridge Philosophical Society, Cambridge University Press.

Gu, Y. J., and L. Shen (2015), Noise correlation tomography of southwest western Canada sedimentary basin, *Geophysical Journal International*, *202*(1), 142-162.

Gupta, H. K. (2018), Reservoir triggered seismicity (RTS) at Koyna, India, over the past 50 yrs, *Bull. Seismol. Soc. Amer.*, *108*(5B), 2907-2918.

Hardebeck, J. L., and E. Hauksson (2001), Crustal stress field in southern California and its implications for fault mechanics, *Journal of Geophysical Research: Solid Earth*, *106*(B10), 21859-21882.

Haug, K., and J. S. Bell (2016), Compilation of In Situ Stress Data from Alberta and Northeastern British Columbia, edited, Alberta Geologcial Survey, Edmonton.

Healy, J., W. Rubey, D. Griggs, and C. Raleigh (1968), The denver earthquakes, *Science*, *161*(3848), 1301-1310.

Heidbach, O., M. Rajabi, K. Reiter, M. Ziegler, and W. team (2016), World stress map database release 2016, *GFZ Data Services*, *10*.

Hincks, T., W. Aspinall, R. Cooke, and T. Gernon (2018), Oklahoma's induced seismicity strongly linked to wastewater injection depth, *Science*, *359*(6381), 1251-1255.

Hoffman, P. F. (1988), United plates of America, the birth of a craton: Early Proterozoic assembly and growth of Laurentia, *Annual Review of Earth and Planetary Sciences*, *16*(1), 543-603.

Jia, S. Q. (2019), Stress Inversion and Damage Quantification in Tight Gas Shale with Application to Hydraulic Fracturing.

Kettlety, T., J. Verdon, M. Werner, and J. Kendall (2020), Stress transfer from opening hydraulic fractures controls the distribution of induced seismicity, *Journal of Geophysical Research: Solid Earth*, *125*(1), e2019JB018794.

King, G. C., R. S. Stein, and J. Lin (1994), Static stress changes and the triggering of earthquakes, *Bull. Seismol. Soc. Amer.*, *84*(3), 935-953.

Kleiner, S., and O. Aniekwe (2019), The Duvernay shale completion journey, paper presented at SPE Kuwait Oil & Gas Show and Conference, Society of Petroleum Engineers.

Lele, S., T. Tyrrell, and G. Dasari (2017), Geomechanical analysis of fault reactivation due to hydraulic fracturing, paper presented at 51st US Rock Mechanics/Geomechanics Symposium, American Rock Mechanics Association.

Lemieux, S. (1999), Seismic reflection expression and tectonic significance of Late Cretaceous extensional faulting of the Western Canada Sedimentary Basin in southern Alberta, *Bulletin of Canadian Petroleum Geology*, *47*(4), 375-390.

Liu, L., and M. D. Zoback (1992), The effect of topography on the state of stress in the crust: application to the site of the Cajon Pass Scientific Drilling Project, *Journal of Geophysical Research: Solid Earth*, *97*(B4), 5095-5108.

MacKay, M. K., D. W. Eaton, P. K. Pedersen, and C. R. Clarkson (2018), Integration of outcrop, subsurface, and microseismic interpretation for rock-mass characterization: An example from the Duvernay Formation, Western Canada, *Interpretation*, *6*(4), T919-T936.

Maury, V., J.-R. Grassob, and G. Wittlinger (1992), Monitoring of subsidence and induced seismicity in the Lacq gas field (France): the consequences on gas production and field operation, *Engineering Geology*, *32*(3), 123-135.

McClure, M. W., and R. N. Horne (2011), Investigation of injection-induced seismicity using a coupled fluid flow and rate/state friction model, *Geophysics*, *76*(6), WC181-WC198.

McLellan, P. (1989), *In-situ stress magnitudes from hydraulic fracturing treatment records: a feasibility study*, Institute of Sedimentary and Petroleum Geology.

Michael, A. J. (1984), Determination of stress from slip data: faults and folds, *Journal of Geophysical Research: Solid Earth*, *89*(B13), 11517-11526.

Moore, P. F. (1988), Devonian reefs in Canada and some adjacent areas.

Morris, A., D. A. Ferrill, and D. B. Henderson (1996), Slip-tendency analysis and fault reactivation, *Geology*, *24*(3), 275-278.

Mukuhira, Y., C. Dinske, H. Asanuma, T. Ito, and M. Häring (2017), Pore pressure behavior at the shut-in phase and causality of large induced seismicity at Basel, Switzerland, *Journal of Geophysical Research: Solid Earth*, *122*(1), 411-435.

Ong, O. N., D. R. Schmitt, and R. S. Kofman (2015), Seismic anisotropy and uniaxial stress measurements on Duvernay sedimentary rocks in Alberta: Report submitted to AER Core Research Laboratory*Rep.*, 28 pp, Alberta Geological Survey, Edmonton.

Ong, O. N., D. R. Schmitt, R. S. Kofman, and K. Haug (2016), Static and dynamic pressure sensitivity anisotropy of a calcareous shale, *Geophys. Prospect.*, *64*(Advances in Rock Physics), 875-897.

Pană, D. I., and B. A. van der Pluijm (2015), Orogenic pulses in the Alberta Rocky Mountains: Radiometric dating of major faults and comparison with the regional tectono-stratigraphic record, *Bulletin*, *127*(3-4), 480-502.

Passelègue, F. X., M. Almakari, P. Dublanchet, F. Barras, J. Fortin, and M. Violay (2020), Initial effective stress controls the nature of earthquakes, *Nature Communications*, *11*(1), 1-8.

Pawley, S., R. Schultz, T. Playter, H. Corlett, T. Shipman, S. Lyster, and T. Hauck (2018), The geological susceptibility of induced earthquakes in the Duvernay play, *Geophysical Research Letters*, *45*(4), 1786-1793.

Peters, S. E., and R. R. Gaines (2012), Formation of the 'Great Unconformity' as a trigger for the Cambrian explosion, *Nature*, *484*(7394), 363-366, doi:10.1038/nature10969.

Pollard, D. D., and P. Segall (1987), Theoretical displacements and stresses near fractures in rock: with applications to faults, joints, veins, dikes, and solution surfaces, paper presented at Fracture mechanics of rock.

Preston, A., G. Garner, K. Beavis, O. Sadiq, and S. Stricker (2016), Duvernay reserves and resources report: A comprehensive analysis of Alberta's foremost liquids-rich shale resource, *Alberta Energy Regulator*, *Calgary*, 83.

Price, R. (2001), An evaluation of models for the kinematic evolution of thrust and fold belts: structural analysis of a transverse fault zone in the Front Ranges of the Canadian Rockies north of Banff, Alberta, *Journal of Structural Geology*, *23*(6-7), 1079-1088.

Rebollar, C., E. Kanasewich, and E. Nyland (1982), Source parameters from shallow events in the Rocky Mountain House earthquake swarm, *Canadian Journal of Earth Sciences*, *19*(5), 907-918.

Reiter, K., O. Heidbach, D. Schmitt, K. Haug, M. Ziegler, and I. Moeck (2014), A revised crustal stress orientation database for Canada, *Tectonophysics*, *636*, 111-124.

Rokosh, C., J. Pawlowicz, H. Berhane, S. Anderson, and A. Beaton (2009), What is shale gas? An introduction to shale-gas geology in Alberta, *Energy Resource Conservation Board (2008-08), available at: http://ags. gov. ab. ca/publications/abstracts/OFR_2008_08. html*.

Ross, G., and D. Eaton (1999), Basement reactivation in the Alberta Basin: Observational constraints and mechanical rationale, *Bulletin of Canadian Petroleum Geology*, *47*(4), 391-411.

Ross, G., R. Parrish, M. Villeneuve, and S. Bowring (1991), Geophysics and geochronology of the crystalline basement of the Alberta Basin, western Canada, *Canadian Journal of Earth Sciences*, *28*(4), 512-522.

Schmitt, D. R. (2014), Basic geomechanics for induced seismicity: A tutorial, *CSEG Recorder (Nov 2014)*, *39*(11), 20-27.

Schmitt, D. R., C. A. Currie, and L. Zhang (2012), Crustal stress determination from boreholes and rock cores: Fundamental principles, *Tectonophysics*, *580*, 1-26.

Schmitt, D. R., and B. Haimson (2017), Hydraulic fracturing stress measurements in deep holes, *Rock Mechanics and Engineering Volume 1: Principles*, 183.

Schultz, R., G. Atkinson, D. Eaton, Y. Gu, and H. Kao (2018), Hydraulic fracturing volume is associated with induced earthquake productivity in the Duvernay play, *Science*, *359*(6373), 304-308.

Schultz, R., R. J. Skoumal, M. R. Brudzinski, D. Eaton, B. Baptie, and W. Ellsworth (2020), Hydraulic Fracturing-Induced Seismicity, *Reviews of Geophysics*, *58*(3), e2019RG000695.

Schultz, R., V. Stern, and Y. J. Gu (2014), An investigation of seismicity clustered near the Cordel Field, west central Alberta, and its relation to a nearby disposal well, *Journal of Geophysical Research: Solid Earth*, *119*(4), 3410-3423.

Schultz, R., V. Stern, Y. J. Gu, and D. Eaton (2015), Detection threshold and location resolution of the Alberta Geological Survey earthquake catalogue, *Seismological Research Letters*, *86*(2A), 385-397.

Schultz, R., and R. Wang (2020), Newly emerging cases of hydraulic fracturing induced seismicity in the Duvernay East Shale Basin, *Tectonophysics*, 228393.

Schultz, R., R. Wang, Y. J. Gu, K. Haug, and G. Atkinson (2017), A seismological overview of the induced earthquakes in the Duvernay play near Fox Creek, Alberta, *Journal of Geophysical Research: Solid Earth*, *122*(1), 492-505.

Schultz, S., J. A. MacEachern, and H. D. Gibson (2019), Late Mesozoic reactivation of Precambrian basement structures and their resulting effects on the sequence stratigraphic architecture of the Viking Formation of east-central Alberta, Canada, *Lithosphere*, *11*(3), 308-321.

Schwab, D. R., T. S. Bidgoli, and M. H. Taylor (2017), Characterizing the Potential for Injection-Induced Fault Reactivation Through Subsurface Structural Mapping and Stress Field Analysis, Wellington Field, Sumner County, Kansas, *Journal of Geophysical Research: Solid Earth*, *122*(12).

Segall, P. (1985), Stress and subsidence resulting from subsurface fluid withdrawal in the epicentral region of the 1983 Coalinga earthquake, *Journal of Geophysical Research: Solid Earth*, *90*(B8), 6801-6816.

Segall, P., and S. Lu (2015), Injection-induced seismicity: Poroelastic and earthquake nucleation effects, *Journal of Geophysical Research: Solid Earth*, *120*(7), 5082-5103.

Seithel, R., E. Gaucher, B. Mueller, U. Steiner, and T. Kohl (2019), Probability of fault reactivation in the Bavarian Molasse Basin, *Geothermics*, *82*, 81-90.

Shapiro, S. A., and C. Dinske (2009), Fluid-induced seismicity: Pressure diffusion and hydraulic fracturing, *Geophys. Prospect.*, *57*(2), 301-310.

Shen, L., D. R. Schmitt, and K. Haug (2018), Measurements of the States of In Situ Stress for the Duvernay Formation near Fox Creek, West-Central Alberta*Rep.*, 29 pp, Alberta Energy Regulator / Alberta Geological Survey.

Shen, L., D. R. Schmitt, and K. Haug (2019a), Quantitative constraints to the complete state of stress from the combined borehole and focal mechanism inversions: Fox Creek, Alberta, *Tectonophysics*, *764*, 13, doi:https://doi.org/10.1016/j.tecto.2019.04.023.

Shen, L., D. R. Schmitt, and R. Schultz (2019b), Frictional Stabilities on Induced Earthquake Fault Planes at Fox Creek, Alberta: A Pore Fluid Pressure Dilemma, *Geophysical Research Letters*, *46*(15), 9, doi:10.1029/2019GL083566.

Shipman, T., R. MacDonald, and T. Byrnes (2018), Experiences and learnings from induced seismicity regulation in Alberta, *Interpretation*, *6*(2), SE15-SE21.

Stein, S., R. Geller, and M. Liu (2011), Bad assumptions or bad luck: Why earthquake hazard maps need objective testing, *Seismological Research Letters*, *82*(5), 623-626.

Stein, S., R. J. Geller, and M. Liu (2012), Why earthquake hazard maps often fail and what to do about it, *Tectonophysics*, *562*, 1-25.

Stork, A., C. Nixon, C. Hawkes, C. Birnie, D. White, D. Schmitt, and B. Roberts (2018), Is CO2 injection at Aquistore aseismic? A combined seismological and geomechanical study of early injection operations, *Int. J. Greenh. Gas Control*, *75*, 107-124.

Streit, J. E., and R. R. Hillis (2004), Estimating fault stability and sustainable fluid pressures for underground storage of CO2 in porous rock, *Energy*, *29*(9-10), 1445-1456.

Suckale, J. (2009), Induced seismicity in hydrocarbon fields, in *Advances in geophysics*, edited, pp. 55-106, Elsevier.

USGS (2020), Search Earthquake Catalog, edited, USGS.

Valley, B., and K. F. Evans (2019), Stress magnitudes in the Basel enhanced geothermal system, *International Journal of Rock Mechanics and Mining Sciences*, *118*, 1-20, doi:10.1016/j.ijrmms.2019.03.008.

van Thienen-Visser, K., and J. Breunese (2015), Induced seismicity of the Groningen gas field: History and recent developments, *The Leading Edge*, *34*(6), 664-671.

Vavryčuk, V. (2014), Iterative joint inversion for stress and fault orientations from focal mechanisms, *Geophysical Journal International*, *199*(1), 69-77.

Wallace, R. E. (1951), Geometry of shearing stress and relation to faulting, *The Journal of geology*, *59*(2), 118-130.

Walsh, F. R., and M. D. Zoback (2016), Probabilistic assessment of potential fault slip related to injection-induced earthquakes: Application to north-central Oklahoma, USA, *Geology*, *44*(12), 991-994.

Warpinski, N. R. (2000), Analytic crack solutions for tilt fields around hydraulic fractures, *Journal of Geophysical Research: Solid Earth*, *105*(B10), 23463-23478.

Weides, S. N., I. S. Moeck, D. R. Schmitt, and J. A. Majorowicz (2014), An integrative geothermal resource assessment study for the siliciclastic Granite Wash Unit, northwestern Alberta (Canada), *Environ. Earth Sci.*, *72*(10), 4141-4154.

Weir, R. M., D. W. Eaton, L. R. Lines, D. C. Lawton, and E. Ekpo (2018), Inversion and interpretation of seismic-derived rock properties in the Duvernay play, *Interpretation-a Journal of Subsurface Characterization*, *6*(2), SE1-SE14, doi:10.1190/int-2017-0149.1.

Wetmiller, R. J. (1986), Earthquakes near Rocky Mountain House, Alberta, and their relationship to gas production facilities, *Canadian Journal of Earth Sciences*, *23*(2), 172-181.

Wilson, M., F. Worrall, R. Davies, and S. Almond (2018), Fracking: How far from faults?, *Geomechanics and Geophysics for Geo-Energy and Geo-Resources*, *4*(2), 193-199.

Woodland, D., and J. Bell (1989), In situ stress magnitudes from mini-frac records in Western Canada, *Journal of Canadian Petroleum Technology*, *28*(05).

Yaghoubi, A., M. Dusseault, S. Mahbaz, and Y. Leonenko (2020), Probabilistic Injection-Induced Fault Slip Assessment in Fox Creek Alberta, paper presented at *54th US Rock Mechanics/Geomechanics Symposium*, American Rock Mechanics Association.

Zang, A., V. Oye, P. Jousset, N. Deichmann, R. Gritto, A. McGarr, E. Majer, and D. Bruhn (2014), Analysis of induced seismicity in geothermal reservoirs–An overview, *Geothermics*, *52*, 6-21.